Jyväskylän yliopiston julkaisuarkisto
Jyväskylä University Digital Archive

UNIVERSITY OF JYVÄSKYLÄ

This is an electronic reprint of the original article.
This reprint *may differ* from the original in pagination and typographic detail.

Author(s): ALICE Collaboration

Title: D-meson production in p-Pb collisions at √sNN = 5.02 TeV and in pp collisions at √s = 7 TeV

Year: 2016

Version:

Please cite the original version:

ALICE Collaboration. (2016). D-meson production in p-Pb collisions at √sNN = 5.02 TeV and in pp collisions at √s = 7 TeV. Physical Review C, 94(5), Article 054908. https://doi.org/10.1103/PhysRevC.94.054908

All material supplied via JYX is protected by copyright and other intellectual property rights, and duplication or sale of all or part of any of the repository collections is not permitted, except that material may be duplicated by you for your research use or educational purposes in electronic or print form. You must obtain permission for any other use. Electronic or print copies may not be offered, whether for sale or otherwise to anyone who is not an authorised user.

PHYSICAL REVIEW C **94**, 054908 (2016)

D-meson production in p-Pb collisions at $\sqrt{s_{NN}} = 5.02$ TeV and in pp collisions at $\sqrt{s} = 7$ TeV

J. Adam *et al.*[*]
(ALICE Collaboration)

(Received 7 June 2016; published 23 November 2016)

Background: In the context of the investigation of the quark gluon plasma produced in heavy-ion collisions, hadrons containing heavy (charm or beauty) quarks play a special role for the characterization of the hot and dense medium created in the interaction. The measurement of the production of charm and beauty hadrons in proton–proton collisions, besides providing the necessary reference for the studies in heavy-ion reactions, constitutes an important test of perturbative quantum chromodynamics (pQCD) calculations. Heavy-flavor production in proton–nucleus collisions is sensitive to the various effects related to the presence of nuclei in the colliding system, commonly denoted cold-nuclear-matter effects. Most of these effects are expected to modify open-charm production at low transverse momenta (p_{T}) and, so far, no measurement of D-meson production down to zero transverse momentum was available at mid-rapidity at the energies attained at the CERN Large Hadron Collider (LHC).

Purpose: The measurements of the production cross sections of promptly produced charmed mesons in p-Pb collisions at the LHC down to $p_{\mathrm{T}} = 0$ and the comparison to the results from pp interactions are aimed at the assessment of cold-nuclear-matter effects on open-charm production, which is crucial for the interpretation of the results from Pb-Pb collisions.

Methods: The prompt charmed mesons D^0, D^+, D^{*+}, and D_s^+ were measured at mid-rapidity in p-Pb collisions at a center-of-mass energy per nucleon pair $\sqrt{s_{NN}} = 5.02$ TeV with the ALICE detector at the LHC. D mesons were reconstructed from their decays $D^0 \to K^-\pi^+$, $D^+ \to K^-\pi^+\pi^+$, $D^{*+} \to D^0\pi^+$, $D_s^+ \to \phi\pi^+ \to K^-K^+\pi^+$, and their charge conjugates, using an analysis method based on the selection of decay topologies displaced from the interaction vertex. In addition, the prompt D^0 production cross section was measured in pp collisions at $\sqrt{s} = 7$ TeV and p-Pb collisions at $\sqrt{s_{NN}} = 5.02$ TeV down to $p_{\mathrm{T}} = 0$ using an analysis technique that is based on the estimation and subtraction of the combinatorial background, without reconstruction of the D^0 decay vertex.

Results: The production cross section in pp collisions is described within uncertainties by different implementations of pQCD calculations down to $p_{\mathrm{T}} = 0$. This allowed also a determination of the total $c\bar{c}$ production cross section in pp collisions, which is more precise than previous ALICE measurements because it is not affected by uncertainties owing to the extrapolation to $p_{\mathrm{T}} = 0$. The nuclear modification factor $R_{p\mathrm{Pb}}(p_{\mathrm{T}})$, defined as the ratio of the p_{T}-differential D meson cross section in p-Pb collisions and that in pp collisions scaled by the mass number of the Pb nucleus, was calculated for the four D-meson species and found to be compatible with unity within uncertainties. The results are compared to theoretical calculations that include cold-nuclear-matter effects and to transport model calculations incorporating the interactions of charm quarks with an expanding deconfined medium.

Conclusions: These measurements add experimental evidence that the modification of the D-meson transverse momentum distributions observed in Pb–Pb collisions with respect to pp interactions is due to strong final-state effects induced by the interactions of the charm quarks with the hot and dense partonic medium created in ultrarelativistic heavy-ion collisions. The current precision of the measurement does not allow us to draw conclusions on the role of the different cold-nuclear-matter effects and on the possible presence of additional hot-medium effects in p-Pb collisions. However, the analysis technique without decay-vertex reconstruction, applied on future larger data samples, should provide access to the physics-rich range down to $p_{\mathrm{T}} = 0$.

DOI: 10.1103/PhysRevC.94.054908

I. INTRODUCTION

The measurement of the production cross section of hadrons containing heavy quarks, charm and beauty, in proton-proton (pp) collisions is a sensitive test of perturbative quantum chromodynamics (pQCD) calculations. The inclusive transverse-momentum (p_{T}) and rapidity (y) differential cross sections can be calculated in the collinear factorization approach as a convolution of three terms: (i) the parton distribution functions (PDF) of the incoming protons; (ii) the partonic hard scattering cross section; and (iii) the fragmentation function, which models the nonperturbative transition of a heavy quark to a given heavy-flavor hadron species [1]. At the energies attained at the CERN Large Hadron Collider (LHC), implementations of these calculations are available at next-to-leading-order (NLO) accuracy in the general-mass variable-flavor-number scheme (GM-VFNS) [2–4] and at fixed order with next-to-leading-log resummation (FONLL) [5,6]. Calculations of heavy-flavor

[*]Full author list given at the end of the article.

Published by the American Physical Society under the terms of the Creative Commons Attribution 3.0 License. Further distribution of this work must maintain attribution to the author(s) and the published article's title, journal citation, and DOI.

 ©2016 CERN, for the ALICE Collaboration

production cross sections in hadronic collisions also exist within the framework of k_T factorization, at leading-order (LO) approximation, with unintegrated gluon distributions (UGDFs) to account for the transverse momenta of the initial partons [7–9]. At energies available at the LHC, the measurement of charm production at low-p_T probes the parton distribution functions of the proton at small values of parton fractional momentum x and squared momentum transfer Q^2. For illustration, in the simplified scenario of a $2 \rightarrow 2$ process at leading order, charm quarks ($m_c \approx 1.5$ GeV/c^2) with $p_T = 0.5$ GeV/c and rapidity $y = 0$ probe the parton distribution functions at $x \approx 4\times10^{-4}$ and $Q^2 \approx 10$ GeV^2. Perturbative QCD calculations have substantial uncertainties at low p_T, owing both to the large effect of the choice of the factorization and renormalization scales at low Q^2 and to the sizable uncertainties on the gluon PDFs at small x [10]. Therefore, a precise measurement of the D-meson production cross section down to $p_T = 0$ could provide an important constraint to pQCD calculations and to low-x gluon PDFs. This is also relevant for cosmic-ray and neutrino astrophysics, where high-energy neutrinos from the decay of charmed hadrons produced in particle showers in the atmosphere constitute an important background for neutrinos from astrophysical sources [11–14]. Furthermore, the measurement in pp collisions provides the reference for results in heavy-ion collisions, where heavy quarks are sensitive probes of the properties of the hot and dense medium with partonic degrees of freedom formed in the collision: The quark-gluon plasma. In this context, the measurement of D-meson production down to $p_T = 0$ in pp collisions also allows the precise determination of the total charm-production cross section, which is a crucial ingredient for the models of charmonium regeneration in the quark-gluon plasma [15–17].

Measurements in proton-nucleus collisions allow an assessment of the various effects related to the presence of nuclei in the colliding system and denoted as cold-nuclear-matter (CNM) effects. In the initial state, the PDFs are modified in bound nucleons as compared to free nucleons, depending on x and Q^2 [18,19]. At energies available at the LHC, the most relevant effect is shadowing: A reduction of the parton densities at low x, which becomes stronger when Q^2 decreases and the nucleus mass number A increases. This effect, induced by the high phase-space density of small-x partons, can be described, within the collinear factorization framework, by means of phenomenological parametrizations of the modification of the PDFs (denoted as nPDFs) [20–22]. If the parton phase-space reaches saturation, PDF evolution equations are not applicable and the most appropriate theoretical description is the color glass condensate effective theory (CGC) [23–27]. The modification of the small-x parton dynamics can significantly reduce D-meson production at low p_T. Furthermore, the multiple scattering of partons in the nucleus before and/or after the hard scattering can modify the kinematic distribution of the produced hadrons: Partons can lose energy in the initial stages of the collision via initial-state radiation [28], or experience transverse momentum broadening owing to multiple soft collisions before the heavy-quark pair is produced [29–31]. These initial-state effects are expected to have a small impact on D-meson production at high p_T ($p_T > 3$–4 GeV/c), but they can induce a significant modification of the D-meson cross section and momentum distribution at lower momenta. For this reason, a measurement of the D-meson production cross section and its nuclear modification factor $R_{p\mathrm{Pb}}$ (the ratio of the cross section in p-Pb collisions to that in pp interactions scaled by the mass number of the Pb nucleus) down to $p_T = 0$ could provide important information. In addition to the initial-state effects discussed above, also final-state effects may be responsible for a modification of heavy-flavor hadron yields and momentum distributions. The presence of significant final-state effects in high-multiplicity p-Pb collisions is suggested by different observations, e.g., the presence of long-range correlations of charged hadrons [32–36], the evolution with multiplicity of the identified-hadron transverse-momentum distributions [37,38], and the suppression of the $\psi(2S)$ production with respect to the J/ψ one [39–41]. The correlation measurements can be described by hydrodynamic calculations assuming the formation of a medium with some degree of collectivity (see, e.g., Refs. [42,43]), even though alternative explanations exist, based on the CGC effective theory (see, e.g., Ref. [44]) or on the anisotropic escape probability of partons from the collision zone [45]. If a collective expansion in the final state were present, the medium could also impart a flow to heavy-flavor hadrons. The possible effect on the D-meson transverse-momentum distributions was first estimated in Ref. [46] by employing an approach based on a blast-wave function with parameters extracted from fits to the light-hadron spectra. More detailed calculations were subsequently carried out in the framework of transport models assuming that also in p-Pb collisions at energies available at the LHC a hot and deconfined medium is formed, which modifies the propagation and hadronization of heavy quarks [47,48]. The results of these calculations show a modification of the D-meson p_T distributions at $p_T < 4$ GeV/c by radial flow, possibly accompanied by a moderate (<20%–30%) suppression at higher p_T, caused by in-medium energy loss.

In this article, we report on the measurements of production cross sections and nuclear modification factors of D mesons performed in minimum-bias p-Pb collisions at $\sqrt{s_{NN}} = 5.02$ TeV with the ALICE detector. In Ref. [49], the results of p_T-differential cross sections and $R_{p\mathrm{Pb}}$ of D^0, D^+, and D^{*+} mesons for $p_T > 1$ GeV/c and of D_s^+ mesons for $p_T > 2$ GeV/c at midrapidity were reported. We complement them in this article with measurements of production cross sections of D^0, D^+, and D^{*+} mesons as a function of rapidity in three p_T intervals. For the D^0 meson, we also report an extension down to $p_T = 0$ of the measurements of the p_T-differential production cross sections in p-Pb collisions at $\sqrt{s_{NN}} = 5.02$ TeV and in pp collisions at $\sqrt{s} = 7$ TeV published in Refs. [49,50], respectively. This allowed a determination of the p_T-integrated D^0 cross section at midrapidity, which for pp collisions at $\sqrt{s} = 7$ TeV is more precise than the previous result [50].

The paper is organized as follows. In Sec. II, the ALICE apparatus, its performance, and the data samples used for the measurement are briefly described. The analysis technique utilized for a first set of measurements of D^0, D^+, D^{*+}, and D_s^+ production is presented in Sec. III together with the corrections

and the systematic uncertainties. This analysis technique is based on the reconstruction of the D-meson displaced decay vertex and is, for brevity, indicated as the analysis "with decay-vertex reconstruction" in this article. With this technique the p_T-differential production cross section was measured down to $p_T = 1$ GeV/c both in pp collisions at $\sqrt{s} = 7$ TeV [50] and in p-Pb collisions at $\sqrt{s_{NN}} = 5.02$ TeV [49], as well as in pp and Pb-Pb collisions at $\sqrt{s_{NN}} = 2.76$ TeV [51,52]. To extend the measurement down to $p_T = 0$, where the decay-vertex selection becomes very inefficient, a different analysis technique, which does not exploit the displaced decay-vertex topology, was developed for the D^0-meson reconstruction in pp collisions at $\sqrt{s} = 7$ TeV and in p-Pb collisions at $\sqrt{s_{NN}} = 5.02$ TeV. This analysis technique, denoted as "without decay-vertex reconstruction" throughout this article, is described in Sec. IV. The results are presented and discussed in Sec. V. The cross sections measured in pp collisions are compared to the results of pQCD calculations, while the measurements of the D-meson nuclear modification factor in p-Pb collisions are compared to models including cold- and hot-nuclear-matter effects.

II. APPARATUS AND DATA SAMPLES

The ALICE apparatus [53,54] consists of a central barrel detector covering the pseudorapidity range $|\eta| < 0.9$, a forward muon spectrometer covering the pseudorapidity range $-4.0 < \eta < -2.5$, and a set of detectors at forward and backward rapidities used for triggering and event characterization. In the following, the detectors used for the D-meson analysis are described.

The D mesons are reconstructed in the midrapidity region using the tracking and particle identification capabilities of the central barrel detectors, which are located in a large solenoidal magnet that produces a magnetic field of 0.5 T along the beam direction (z axis). The innermost detector of the central barrel is the inner tracking system (ITS), which is composed of six cylindrical layers of silicon detectors with radii between 3.9 and 43.0 cm. The two innermost layers, with average radii of 3.9 and 7.6 cm, are equipped with silicon pixel detectors (SPD); the two intermediate layers, with average radii of 15.0 and 23.9 cm, are equipped with silicon drift detectors and the two outermost layers, with average radii of 38.0 and 43.0 cm, are equipped with double-sided silicon strip detectors. The low material budget (on average 7.7% of a radiation length for tracks crossing the ITS at $\eta = 0$), the high spatial resolution, and the small distance of the innermost layer from the beam vacuum tube allow the measurement of the track impact parameter in the transverse plane (d_0), i.e., the distance of closest approach of the track to the interaction vertex in the plane transverse to the beam direction, with a resolution better than 75 μm for $p_T > 1$ GeV/c [55].

The ITS is surrounded by a large cylindrical time projection chamber (TPC) [56] with an active radial range from about 85 to 250 cm and an overall length along the beam direction of 500 cm. It covers the full azimuth in the pseudorapidity range $|\eta| < 0.9$ and provides track reconstruction with up to 159 points along the trajectory of a charged particle as well as particle identification via the measurement of specific energy loss dE/dx. The charged-particle identification capability of the TPC is supplemented by the time-of-flight detector (TOF) [57], which is based on multigap resistive plate chambers and is positioned at radial distances between 377 and 399 cm from the beam axis. The TOF detector measures the flight time of the particles from the interaction point. The start time of the event can be determined either from the information provided by the T0 detector [58] or via a combinatorial analysis of the particle arrival times at the TOF detector [57]. The T0 detector is composed of two arrays of Cherenkov counters located on either side of the interaction point at +350 and −70 cm from the nominal vertex position along the beam line. The T0 time resolution is about 40 ps for pp collisions. The overall TOF resolution, including the uncertainty on the start time of the event, and the tracking and momentum resolution contributions, is about 150 ps in pp collisions and 85 ps for high-multiplicity p-Pb collisions [54].

Triggering and event selection are based on the V0 and SPD detectors and on the zero-degree calorimeters (ZDCs). The V0 detector consists of two scintillator arrays, denoted V0A and V0C, covering the pseudorapidity ranges $2.8 < \eta < 5.1$ and $-3.7 < \eta < -1.7$, respectively [59]. The ZDCs are two sets of neutron and proton calorimeters positioned along the beam axis on both sides of the ALICE apparatus at about 110 m from the interaction point.

The data samples used for the analyses presented here include p-Pb collisions at $\sqrt{s_{NN}} = 5.02$ TeV and pp collisions at $\sqrt{s} = 7$ TeV, collected in 2013 and 2010, respectively. During the p-Pb run, the beam energies were 4 TeV for protons and 1.58 TeV per nucleon for lead nuclei. With this beam configuration, the nucleon-nucleon center-of-mass system moves in rapidity by $\Delta y_{\rm cms} = 0.465$ in the direction of the proton beam. The D-meson analyses were performed in the laboratory-frame interval $|y_{\rm lab}| < 0.5$, which leads to a shifted center-of-mass rapidity coverage of $-0.96 < y_{\rm cms} < 0.04$. In p-Pb collisions, minimum-bias events were selected, requiring at least one hit in both the V0A and the V0C scintillator arrays. In pp collisions, minimum-bias events were triggered by requiring at least one hit in either of the V0 counters or in the SPD. The minimum-bias (MB) trigger was estimated to be sensitive to about 96.4% and 87% of the p-Pb and pp inelastic cross sections, respectively [60,61]. Beam-gas and other machine-induced background collisions were removed via off-line selections based on the timing information provided by the V0 and the ZDCs and the correlation between the number of hits and track segments (tracklets) in the SPD detector. For the data samples considered in this paper, the probability of collision pileup was below 4% per triggered pp event and below the percent level per triggered p-Pb event. An algorithm to detect multiple interaction vertices was used to reduce the pileup contribution. An event was rejected if a second interaction vertex was found. The remaining undetected pileup was negligible in the present analysis. Only events with a primary vertex reconstructed within ±10 cm from the center of the detector along the beam line were considered. The number of events passing these selection criteria was about 10^8 for p-Pb collisions and about 3.1×10^8 for pp collisions. The corresponding integrated luminosities, $L_{\rm int} = N_{\rm MB}/\sigma_{\rm MB}$, where $\sigma_{\rm MB}$ is the MB trigger cross section measured with van der Meer scans, are 48.6 μb^{-1}, with an uncertainty of 3.7%,

for the p-Pb sample [60], and 5.0 nb^{-1} ($\pm$3.5%) for the pp sample [61].

III. ANALYSIS WITH DECAY-VERTEX RECONSTRUCTION IN p-Pb COLLISIONS

A. D^0, D^+, D^{*+}, and D_s^+ meson reconstruction and selection

D^0, D^+, D^{*+}, and D_s^+ mesons, and their charge conjugates, were reconstructed via their hadronic decay channels $D^0 \to K^-\pi^+$ [with a branching ratio (BR) of $3.88 \pm 0.05\%$], $D^+ \to K^-\pi^+\pi^+$ (BR $= 9.13 \pm 0.19\%$), $D^{*+} \to D^0\pi^+$ (BR $= 67.7 \pm 0.5\%$) followed by $D^0 \to K^-\pi^+$, and $D_s^+ \to \phi\pi^+ \to K^-K^+\pi^+$ (BR $= 2.24 \pm 0.10\%$) [62]. The D^0, D^+, and D_s^+ mesons decay weakly with mean proper decay lengths ($c\tau$) of about 123, 312, and 150 μm [62], respectively. The analysis strategy was based on the reconstruction of secondary vertices separated by a few hundred μm from the interaction point. The D^{*+} meson decays strongly at the primary vertex, and the decay topology of the produced D^0 was reconstructed along with a soft pion originating from the primary vertex. The transverse momentum of the soft pion produced in the D^{*+} decays typically ranges from 0.1 to 1.5 GeV/c, depending on the D^{*+} p_{T}.

D^0, D^+, and D_s^+ candidates were formed using pairs and triplets of tracks with the correct charge-sign combination. Tracks were selected by requiring $|\eta| < 0.8$, $p_{\mathrm{T}} > 0.3$ GeV/c, at least 70 (of a maximum of 159) associated space points and a fit quality $\chi^2/\mathrm{ndf} < 2$ in the TPC, and at least two (of six) hits in the ITS, of which at least one had to be in either of the two SPD layers. D^{*+} candidates were formed by combining D^0 candidates with tracks with $p_{\mathrm{T}} > 0.1$ GeV/c and at least three hits in the ITS, of which at least one had to be in the SPD. The track selection criteria reduce the D-meson acceptance, which drops steeply to zero for $|y_{\mathrm{lab}}| > 0.5$ at low p_{T} and for $|y_{\mathrm{lab}}| > 0.8$ at $p_{\mathrm{T}} > 5$ GeV/c. A p_{T}-dependent fiducial acceptance region was therefore defined as $|y_{\mathrm{lab}}| < y_{\mathrm{fid}}(p_{\mathrm{T}})$, with $y_{\mathrm{fid}}(p_{\mathrm{T}})$ increasing from 0.5 to 0.8 in the transverse-momentum range $0 < p_{\mathrm{T}} < 5$ GeV/c according to a second-order polynomial function, and $y_{\mathrm{fid}} = 0.8$ for $p_{\mathrm{T}} > 5$ GeV/c.

The selection of the D-meson decay topology was mainly based on the displacement of the tracks from the interaction vertex, the separation of the primary and secondary vertices, and the pointing of the reconstructed D-meson momentum to the primary vertex. A detailed description of the variables used to select the D-meson candidates can be found in Refs. [50,63]. The actual cut values were optimized for the signal and background levels of the p-Pb sample; they depend on the D-meson species and p_{T}, but they are the same in all the considered rapidity intervals.

Further reduction of the combinatorial background was obtained by applying particle identification (PID) to the decay tracks. A 3σ compatibility cut was applied to the difference between the measured and expected signals for pions and kaons for the TPC dE/dx and the time-of-flight measured with the TOF detector. Tracks without hits in the TOF detector were identified using only the TPC information. Particle identification selections were not applied to the pion track from the D^{*+} strong decay. A tighter PID selection was applied to the D_s^+ candidates: Tracks without a TOF signal (mostly at low momentum) were identified using only the TPC information and requiring a 2σ compatibility with the expected dE/dx. This stricter PID selection strategy was needed in the D_s^+ case owing to the large background of track triplets and the short D_s^+ lifetime, which limits the effectiveness of the geometrical selections on the displaced decay-vertex topology. In addition, in the cases of $D^+ \to K^-\pi^+\pi^+$ and $D_s^+ \to K^-K^+\pi^+$ decays, the charge signs of the decay particles were exploited in combination with the pion and kaon identification. Because in both these decay modes the decay particle with the opposite charge sign with respect to the D meson has to be a kaon, a candidate was rejected if the opposite-sign track was not compatible with the kaon hypothesis. The applied PID strategy provides a reduction of the combinatorial background by a factor of about three at low p_{T} while preserving an efficiency of 95% for the D^0, D^+, and D^{*+} signals and of 85% for the D_s^+ signal. The fraction of signal candidates passing the PID selections is lower than that expected from a perfectly Gaussian response owing to the non-Gaussian tail of the TOF signal and the non-negligible contamination originating from wrong associations between reconstructed tracks and TOF hits [64].

In the D_s^+ case, to select $D_s^+ \to \phi\pi^+$ decays with $\phi \to K^-K^+$, candidates were rejected if none of the two pairs of opposite-charge tracks (required to be compatible with the kaon hypothesis) had an invariant mass compatible with the particle data group (PDG) world average for the ϕ meson mass (1.0195 GeV/c^2) [62]. The difference between the reconstructed K^+K^- invariant mass and world-average ϕ mass was required to be less than 5–10 MeV/c^2 depending on the D_s^+ p_{T} interval. This selection preserves 70%–85% of the D_s^+ signal.

The D-meson raw yields were extracted from fits to the D^0, D^+, and D_s^+ candidate invariant-mass distributions and to the mass difference $\Delta M = M(K\pi\pi) - M(K\pi)$ distributions for D^{*+} candidates. In the fit function, the signal is modeled with a Gaussian and the background is described by an exponential term for D^0, D^+, and D_s^+ candidates and by a threshold function multiplied by an exponential ($a\sqrt{\Delta M - m_\pi}e^{b(\Delta M - m_\pi)}$) for the D^{*+} case. For all four D-meson species, the mean values of the Gaussian functions in all transverse momentum and rapidity intervals were found to be compatible within uncertainties with the PDG world-average values [62]. The Gaussian widths are consistent with the simulation results with deviations of at most 15%.

With the analysis based on the decay-vertex reconstruction, D-meson yields were extracted as a function of the transverse momentum in the range $1 < p_{\mathrm{T}} < 24$ GeV/c for D^0, D^+, and D^{*+} ($2 < p_{\mathrm{T}} < 12$ GeV/c for D_s^+) in a rapidity interval $|y_{\mathrm{lab}}| < y_{\mathrm{fid}}(p_{\mathrm{T}})$. The yield of D^0, D^+, and D^{*+} mesons was measured also as a function of rapidity in three p_{T} intervals: $2 < p_{\mathrm{T}} < 5$ GeV/c, $5 < p_{\mathrm{T}} < 8$ GeV/c, and $8 < p_{\mathrm{T}} < 16$ GeV/c. The rapidity interval of the measurement was $|y_{\mathrm{lab}}| < 0.7$ for the lowest p_{T} interval and $|y_{\mathrm{lab}}| < 0.8$ for the other two p_{T} intervals.

Figure 1 shows the D^0, D^+, and D_s^+ candidate invariant-mass distributions and the D^{*+} mass-difference distribution in four p_{T} intervals in the fiducial acceptance region $|y_{\mathrm{lab}}| < y_{\mathrm{fid}}(p_{\mathrm{T}})$. In addition, the invariant-mass (mass-difference)

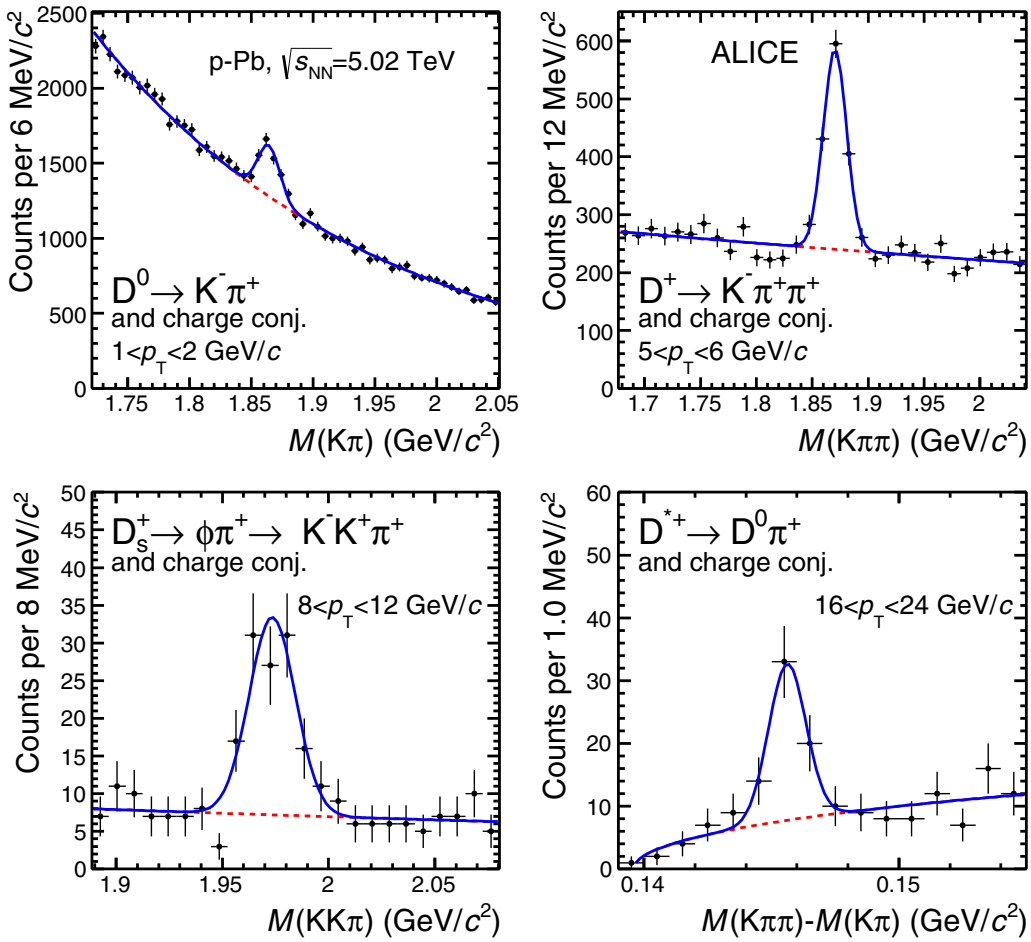

FIG. 1. Distributions of the invariant mass for D^0 (top left), D^+ (top right), and D_s^+ (bottom left) candidates and their charge conjugates and of the mass difference for D^{*+} (bottom right) candidates (and charge conjugates) in the rapidity interval $|y_{\rm lab}| < y_{\rm fid}(p_{\rm T})$ in p-Pb collisions. The dashed lines represent the fit to the background while the solid lines represent the total fit function. One $p_{\rm T}$ interval is shown for each species: $1 < p_{\rm T} < 2$ GeV/c for D^0, $5 < p_{\rm T} < 6$ GeV/c for D^+, $8 < p_{\rm T} < 12$ GeV/c for D_s^+, and $16 < p_{\rm T} < 24$ GeV/c for D^{*+}.

distributions of D^0, D^+, and D^{*+} candidates in two rapidity intervals, namely $|y_{\rm lab}| < 0.1$ and $-0.8 < y_{\rm lab} < -0.4$ ($-0.7 < y_{\rm lab} < -0.4$ for $p_{\rm T} < 5$ GeV/c), are shown in the upper and lower panels of Fig. 2 for three $p_{\rm T}$ intervals.

B. Acceptance, efficiency, and subtraction of beauty feed-down contribution

The D-meson raw yields extracted in each $p_{\rm T}$ and y interval were corrected to obtain the prompt D-meson cross sections:

$$\frac{d^2\sigma^D}{dp_{\rm T}dy} = \frac{1}{\Delta p_{\rm T}} \frac{f_{\rm prompt}\frac{1}{2}N^{D+\overline{D},{\rm raw}}(p_{\rm T})}{\Delta y} \cdot \frac{1}{({\rm Acc}\times\varepsilon)_{\rm prompt}(p_{\rm T})} \frac{1}{{\rm BR}L_{\rm int}}. \quad (1)$$

In the formula, $N^{D+\overline{D},{\rm raw}}$ is the raw yield (sum of particles and antiparticles). It includes contributions from both prompt (i.e., produced in the charm quark fragmentation, either directly or through decays of excited open charm and charmonium states) and from feed-down D mesons (i.e., originating from beauty-hadron decays). The factor $1/2$ accounts for the fact that the measured yields include particles and antiparticles while the cross sections are given for particles only; $f_{\rm prompt}$ is the fraction of prompt D mesons in the raw yield; $({\rm Acc}\times\varepsilon)_{\rm prompt}$ is the product of acceptance and efficiency for prompt D mesons, where ε accounts for primary vertex reconstruction, D-meson decay track reconstruction and selection, and D-meson candidate selection with secondary-vertex and PID cuts; $\Delta p_{\rm T}$ and Δy are the widths of the transverse-momentum and rapidity intervals; BR is the branching ratio of the considered decay channel; and $L_{\rm int}$ is the integrated luminosity.

The acceptance and efficiency correction factors were obtained from Monte Carlo simulations including detailed descriptions of the geometry of the apparatus and of the detector response. Proton-proton collisions were generated by using the PYTHIA v6.4.21 event generator [65] with the Perugia-0 tune [66]. Events containing a $c\overline{c}$ or $b\overline{b}$ pair were selected and an underlying p-Pb collision generated with HIJING 1.36 [67] was added to each of them to obtain a better description of the multiplicity distributions observed in data. The generated D-meson $p_{\rm T}$ distribution was weighted to match the shape predicted by FONLL calculations [5] at $\sqrt{s} =$ 5.02 TeV, based on the observation that FONLL provides a

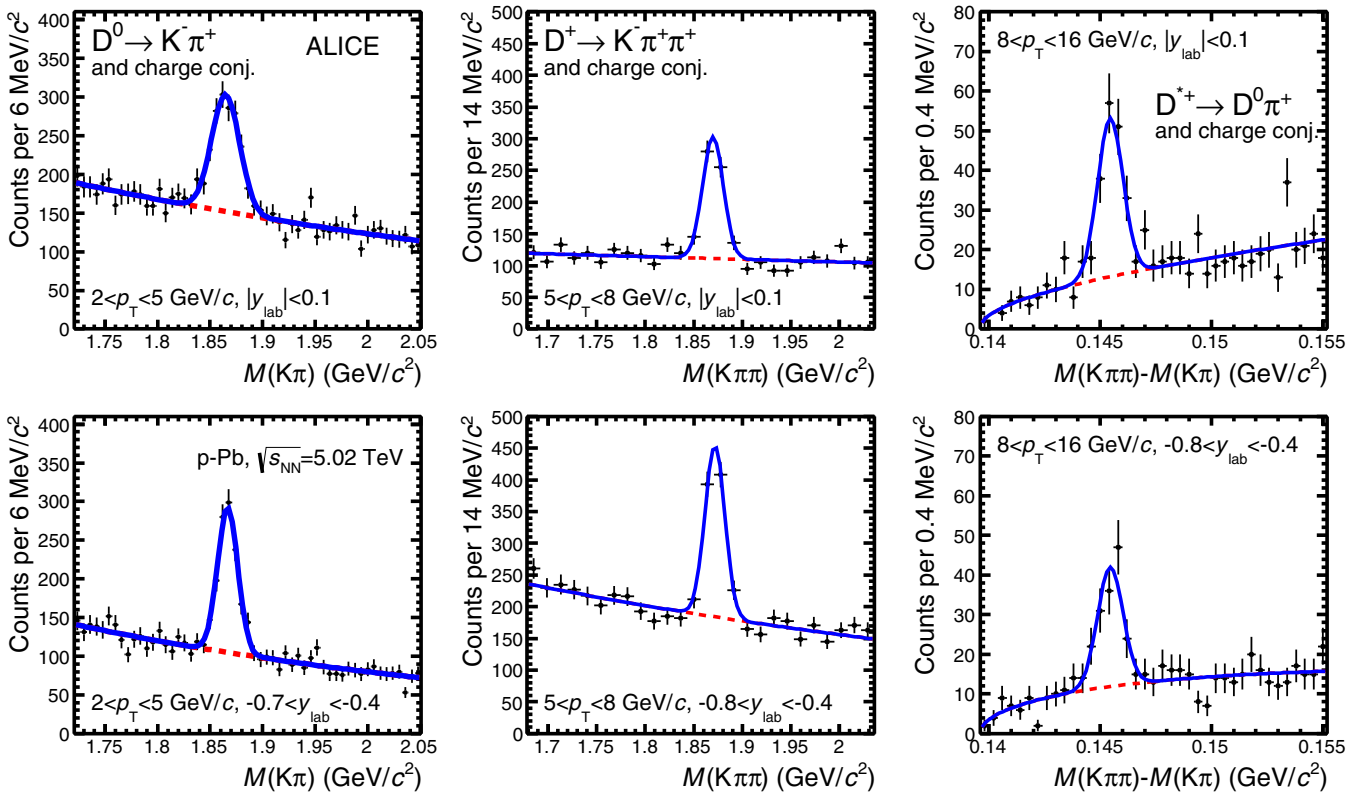

FIG. 2. Distributions of the invariant mass for D^0 (left column) and D^+ (middle column) candidates and their charge conjugates and of the mass difference for D^{*+} (right column) candidates (and charge conjugates) in p-Pb collisions in the rapidity intervals $|y_{\rm lab}| < 0.1$ (top row) and $-0.8 < y_{\rm lab} < -0.4$ ($-0.7 < y_{\rm lab} < -0.4$ for $p_{\rm T} < 5$ GeV/c) (bottom row). The dashed lines represent the fit to the background, while the solid lines represent the total fit function. One $p_{\rm T}$ interval is shown for each species: $2 < p_{\rm T} < 5$ GeV/c for D^0, $5 < p_{\rm T} < 8$ GeV/c for D^+, and $8 < p_{\rm T} < 16$ GeV/c for D^{*+}.

good description of the measured D-meson $p_{\rm T}$-differential cross sections at $\sqrt{s} = 2.76$ and 7 TeV [6,50,51,68].

The efficiency depends on the multiplicity of charged particles produced in the collision, because the primary vertex resolution, thus the resolution for the topological selection variables, improves at high multiplicity. Therefore, the generated events were weighted on the basis of their charged-particle multiplicity to match the multiplicity distribution observed in data. The weight function was defined as the ratio between the distribution of the number of tracklets (segments of tracks connecting two hits in the SPD layers and aligned with the primary vertex) measured in data and that obtained in the Monte Carlo simulation. The efficiency varies from about 1% to 30% depending on D-meson $p_{\rm T}$ and species. As an example, the product of acceptance and efficiency Acc $\times\, \varepsilon$ for prompt D^0 mesons is shown in Fig. 3 (left panel) as a function of $p_{\rm T}$ in the rapidity range $|y_{\rm lab}| < y_{\rm fid}(p_{\rm T})$. In the same figure, the efficiencies when the PID selection is not applied (about 5% higher as expected from the PID strategy utilized) and efficiencies for D^0 mesons from B decays are also shown (about a factor of two higher because the decay vertices of feed-down D mesons are more displaced from the primary vertex and they are more efficiently selected by the topological selections). The figures of Acc $\times\, \varepsilon$ as a function of $p_{\rm T}$ for D^+, D^{*+}, and D_s^+ mesons can be found in Ref. [69]. The right-hand panel of Fig. 3 shows the prompt D^0 Acc $\times\, \varepsilon$ as a function of $y_{\rm lab}$ for the three momentum intervals considered in this analysis. The small decrease at $|y_{\rm lab}| > 0.4$ is attributable to the detector acceptance.

The correction factor $f_{\rm prompt}$ was calculated with a FONLL-based method as

$$\begin{aligned} f_{\rm prompt} &= 1 - \frac{N_{\rm raw}^{D\ \text{feed-down}}}{N_{\rm raw}^{D}} \\ &= 1 - A\left(\frac{d^2\sigma}{dp_{\rm T}dy}\right)_{\text{feed-down}}^{\rm FONLL} R_{p\rm Pb}^{\text{feed-down}} \\ &\quad \times \frac{(\text{Acc}\times\varepsilon)_{\text{feed-down}}\Delta y \Delta p_{\rm T} {\rm BR} L_{\rm int}}{N^{D+\overline{D},\rm raw}/2}, \end{aligned} \tag{2}$$

where A is the mass number of the Pb nucleus. The procedure uses the B-meson production cross section in pp collisions at $\sqrt{s} = 5.02$ TeV estimated with FONLL calculations, the $B \to D + X$ decay kinematics from the EVTGEN package [70], the efficiencies for D mesons from beauty-hadron decays and a hypothesis on the nuclear modification factor $R_{p\rm Pb}^{\text{feed-down}}$ of D mesons from B decays. On the basis of calculations including initial-state effects through the EPS09 nuclear PDF parametrizations [20] or the color glass condensate formalism [27], it was assumed that the $R_{p\rm Pb}$ of prompt and feed-down D mesons were equal and their ratio was varied in the range $0.9 < R_{p\rm Pb}^{\text{feed-down}}/R_{p\rm Pb}^{\rm prompt} < 1.3$ to evaluate the systematic uncertainties. The resulting $f_{\rm prompt}$ values and their

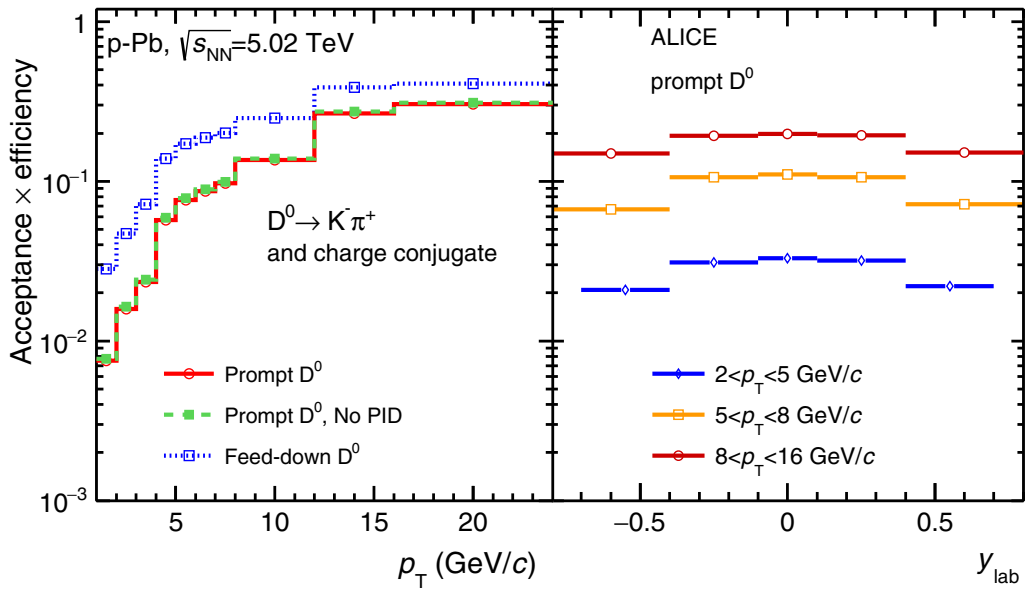

FIG. 3. Product of acceptance and efficiency for D^0 mesons as a function of p_T (left) and as a function of y_{lab} (right). In the left panel, efficiencies are shown for prompt D^0 with (solid line) and without (dashed line) PID selection applied and feed-down D^0 (dotted line). In the right panel, the Acc × ε values are shown for prompt D^0 mesons for the three p_T intervals considered in the analysis as a function of rapidity.

uncertainties are shown in the right-hand panels of Fig. 4 for D^0, D^+, and D^{*+} mesons in the $|y_{lab}| < y_{fid}(p_T)$ interval. The central values of f_{prompt} range between 0.81 and 0.96 depending on D-meson species and p_T with no significant rapidity dependence.

C. Systematic uncertainties

The systematic uncertainties on the raw-yield values were determined for each p_T and y interval by repeating the fit in a different mass range, by varying the background fit function and by counting the candidates in the invariant-mass region of the signal peak after subtracting the background estimated from the sidebands. The alternative background fit functions considered were a linear or a second-order polynomial function for D^0, D^+, and D_s^+ and $a(\Delta M - m_\pi)^b$ for the D^{*+}. For the D^0 meson, the systematic uncertainty on the raw-yield extraction also includes a contribution owing to signal candidates reconstructed when swapping the masses of the final-state kaon and pion (*reflections*). This contribution, which is strongly reduced by the PID selection, was estimated to be 3% (4%) at low (high) p_T based on the invariant-mass distribution of these candidates in the simulation.

For D_s^+ mesons, it was also verified that the contribution to the measured yield owing to other decay channels giving rise to the same $K^-K^+\pi^+$ final state, in particular $D_s^+ \to \overline{K}^{*0}K^+$ and $D_s^+ \to f_0(980)\pi^+$, is completely negligible owing to the much lower efficiency for the selection of these decays induced by the cut on the KK invariant mass in combination with the kaon and pion identification [63].

The systematic uncertainty on the tracking efficiency was estimated by comparing the probability to match the TPC tracks to the ITS hits in data and simulation and by varying the track quality selection criteria. It amounts to 3% for each track, which results in a 6% uncertainty for the two-body decay of D^0 mesons and 9% for D^+, D^{*+}, and D_s^+ mesons, which are reconstructed from three-body final states.

The systematic uncertainty on the D-meson selection efficiency reflects residual discrepancies between data and simulations on the variables used in the displaced decay-vertex topology selection criteria. This effect was estimated by repeating the analysis with different values of the selection cuts, which significantly vary the signal-to-background ratio and efficiencies. The value of the uncertainty was estimated from the variation of the corrected yields. The systematic uncertainties are largest at low p_T, where the efficiencies are lowest, and decrease with increasing p_T, with no dependence on rapidity.

The systematic uncertainty associated with particle identification was estimated for D^0, D^+, and D^{*+} mesons by comparing the corrected yields with and without applying PID to select pions and kaons. The results for the two cases were found to be compatible; therefore, no systematic uncertainty was assigned. In the D_s^+ case, owing to the tighter kaon and pion identification criteria, a PID systematic uncertainty of 10% in the interval $2 < p_T < 4$ GeV/c and 5% at $p_T >$ 4 GeV/c was estimated by varying the PID selection criteria with the procedure described in Ref. [63].

The effect on the efficiencies owing to the shape of the simulated D-meson p_T distribution was evaluated by considering different shapes (PYTHIA, FONLL) and was found to range from 0% to 4% depending on p_T. No significant systematic effect is induced by the rapidity distribution of the generated D mesons because the efficiency does not have a pronounced rapidity dependence. The effect of possible differences between the charged-multiplicity distributions in data and simulations was found to be negligible.

The systematic uncertainty owing to the subtraction of feed-down D mesons from B decays was estimated as in

TABLE I. Relative systematic uncertainties on prompt D-meson production cross sections in p-Pb collisions in two p_T intervals and the rapidity range $|y| < y_{fid}(p_T)$.

	D^0		D^+		D^{*+}		D_s^+	
p_T interval (GeV/c)	1–2	5–6	1–2	5–6	1–2	12–16	2–4	6–8
Raw yield extraction (%)	8	4	10	5	8	2	10	5
Correction factor								
Tracking efficiency (%)	6	6	9	9	9	9	9	9
Selection efficiency (%)	8	5	10	6	10	5	15	15
PID efficiency (%)	Negl.	Negl.	Negl.	Negl.	Negl.	Negl.	10	5
MC p_T shape (%)	2	Negl.	2	Negl.	3	1	4	4
MC N_{ch} shape (%)	Negl.	Negl.	Negl.	Negl.	Negl.	Negl.	Negl.	Negl.
Feed-down from B (%)	$^{+5}_{-47}$	$^{+5}_{-12}$	$^{+1}_{-22}$	$^{+3}_{-7}$	$^{+2}_{-30}$	$^{+2}_{-5}$	$^{+4}_{-24}$	$^{+7}_{-14}$
Luminosity (%)	3.7		3.7		3.7		3.7	
Branching ratio (%)	1.3		2.1		1.5		4.5	

previous measurements [50] by varying the FONLL parameters (b-quark mass, factorization and renormalization scales) as prescribed in Ref. [6] and by varying the hypothesis on the $R_{p\mathrm{Pb}}^{\text{feed-down}}$ as described in Sec. III B. An alternative method based on the ratio of FONLL predictions for D- and B-meson cross sections was also used [50].

The cross sections have a systematic uncertainty on the normalization induced by the uncertainties on the integrated luminosity (3.7% [60]) and on the branching ratios of the considered D-meson decays.

A summary of the systematic uncertainties is reported in Tables I and II. The systematic uncertainties on PID, tracking, and selection efficiencies are mostly correlated among the different p_T and rapidity intervals, while the raw-yield extraction uncertainty is mostly uncorrelated.

D. Prompt fraction with a data-driven approach

The prompt fractions in the raw yields of D^0, D^+, and D^{*+} mesons, f_{prompt}, calculated with the FONLL-based method of Eq. (2) were cross checked with a data-driven method that exploits the different shapes of the distributions of the transverse-plane impact parameter to the primary vertex (d_0) of prompt and feed-down D mesons. The prompt fraction was estimated via an unbinned likelihood fit of the d_0 distribution of $D^0(D^+)$-meson candidates with invariant mass $|M - M_D| < 1.5(2)\sigma$ (where σ is the width of the Gaussian function describing the D-meson signal in the invariant-mass fits) and of D^{*+}-meson candidates with a mass difference $|\Delta M - \Delta M_{D^{*+}}| < 2.5\sigma$, using the fit function

$$F(d_0) = S[(1 - f_{\text{prompt}})F^{\text{feed-down}}(d_0) + f_{\text{prompt}}F^{\text{prompt}}(d_0)] + BF^{\text{backgr}}(d_0). \quad (3)$$

In this function, S and B are the signal raw yield and background in the selected invariant-mass range; and $F^{\text{prompt}}(d_0)$, $F^{\text{feed-down}}(d_0)$, and $F^{\text{backgr}}(d_0)$ are functions describing the impact-parameter distributions of prompt D mesons, feed-down D mesons, and background, respectively. The function F^{prompt} is a detector-resolution term modeled with a Gaussian and a symmetric exponential term, $\frac{1}{2\lambda}\exp(-\frac{|d_0|}{\lambda})$, describing the tails of the impact-parameter distribution of prompt D mesons. $F^{\text{feed-down}}$ is the convolution of the detector-resolution term with a symmetric double-exponential function ($F_{\text{true}}^{\text{feed-down}}$) describing the intrinsic impact-parameter distribution of secondary D mesons from B-meson decays, which is determined by the decay length and decay kinematics of B mesons. The parameters of the F^{prompt} and $F_{\text{true}}^{\text{feed-down}}$ functions were fixed to the values obtained by fitting the distributions

TABLE II. Relative systematic uncertainties on prompt D-meson production cross sections in p-Pb collisions in the p_T interval $5 < p_T < 8$ GeV/c and two rapidity intervals.

	D^0		D^+		D^{*+}	
y_{lab} interval	−0.1,0.1	0.4, 0.8	−0.1,0.1	0.4, 0.8	−0.1,0.1	0.4, 0.8
Raw yield extraction (%)	10	6	5	5	3	6
Correction factor						
Tracking efficiency (%)	6	6	9	9	9	9
Selection efficiency (%)	5	5	8	8	5	5
PID efficiency (%)	Negl.	Negl.	Negl.	Negl.	Negl.	Negl.
MC p_T shape (%)	3	3	5	5	5	5
MC N_{ch} shape (%)	Negl.	Negl.	Negl.	Negl.	Negl.	Negl.
Feed-down from B (%)	$^{+5}_{-11}$	$^{+5}_{-11}$	$^{+3}_{-7}$	$^{+3}_{-7}$	$^{+2}_{-5}$	$^{+2}_{-4}$
Luminosity (%)	3.7		3.7		3.7	
Branching ratio (%)	1.3		2.1		4.5	

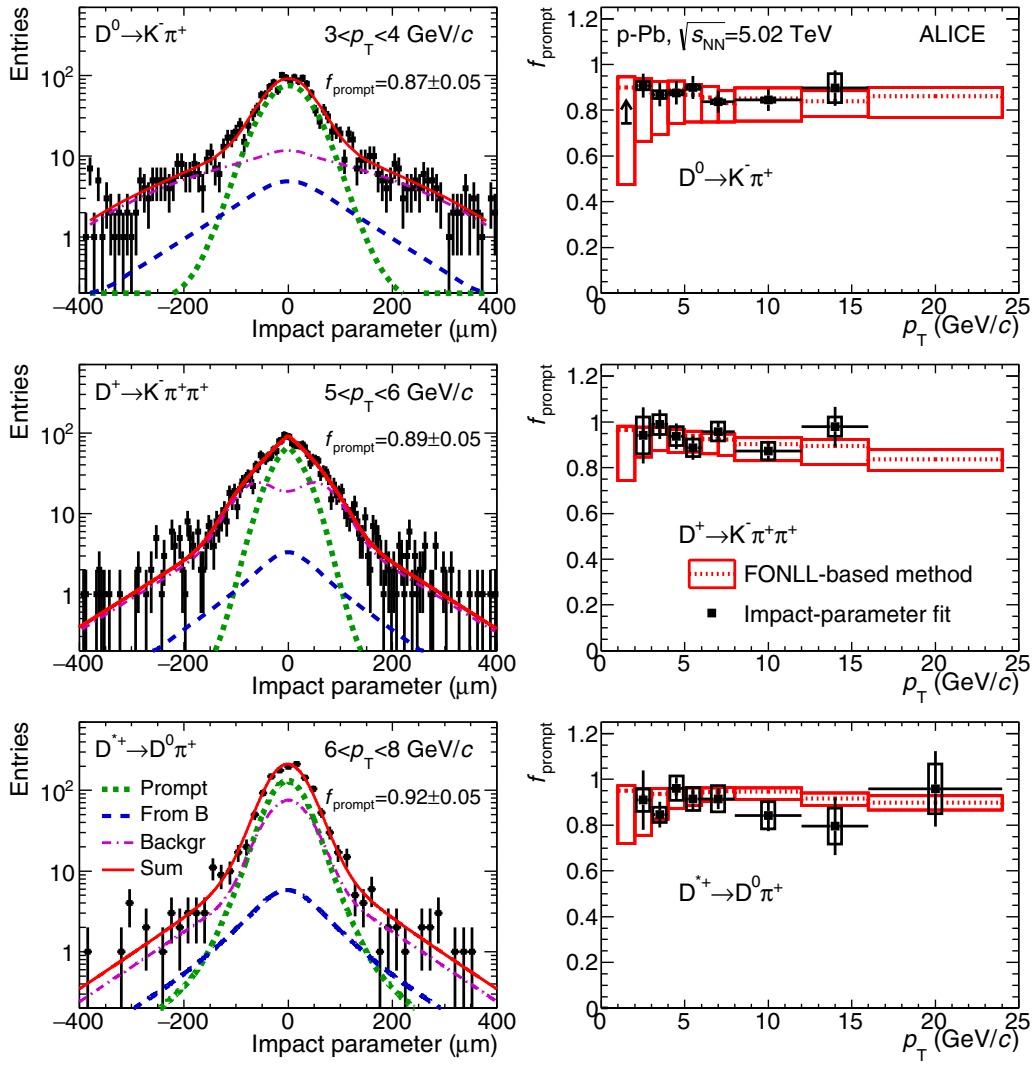

FIG. 4. (Left) Examples of fits to D^0 (top), D^+ (middle), and D^{*+} (bottom) impact-parameter distributions in the p_T intervals $3 < p_T < 4$ GeV/c, $5 < p_T < 6$ GeV/c, and $6 < p_T < 8$ GeV/c, respectively. The curves show the fit functions describing the prompt, feed-down, and background contributions, as well as their sum, as described in the text. (Right) Fraction of prompt D^0 (top), D^+ (middle), and D^{*+} (bottom) raw yield as a function of p_T compared to the FONLL-based approach. The results from the data-driven method are shown as square markers with the error bars (boxes) representing the statistical (systematic) uncertainty. The arrow in the interval $1 < p_T < 2$ GeV/c represents the minimum value within a 95% confidence level. The central values of f_{prompt} from the FONLL-based approach are shown by the dashed line and their uncertainty by the red boxes.

from Monte Carlo simulations, except for the Gaussian width of the detector-resolution term, which was kept free in the data fit to compensate for a possible imperfect description of the impact-parameter resolution in the simulation. The widths recovered from the fit to the data were found to be in agreement with the simulation for $p_T > 3$ GeV/c and slightly larger at lower p_T. For D^0 and D^{*+} mesons, the background fit function, F^{backgr}, is the sum of a Gaussian and a symmetric exponential term centered at zero. For D^+ mesons, the background impact-parameter distribution has a double-peak structure with a depletion around zero induced by the selections applied. The shape was thus modeled with two Gaussians and two symmetric exponential terms. The parameters of F^{backgr} were fixed by fitting the impact-parameter distribution of background candidates in the sidebands of the signal peak in the invariant-mass distributions (mass difference for D^{*+} mesons), namely in the interval $4\sigma < |M - M_{D^0,D^+}| < 15\sigma$ ($6\sigma < \Delta M - \Delta M_{D^{*+}} < 15\sigma$). Figure 4 (left) shows examples of fits to the impact-parameter distributions of D^0, D^+, and D^{*+} mesons in the transverse-momentum intervals $3 < p_T < 4$ GeV/c, $5 < p_T < 6$ GeV/c, and $6 < p_T < 8$ GeV/c, respectively.

The prompt fraction estimated with the data-driven approach has systematic uncertainties owing to (i) the shape assumed for prompt D-meson, feed-down D-meson, and background impact-parameter distributions, (ii) the uncertainty on the signal and background yields, and (iii) the consistency of the procedure, evaluated with a Monte Carlo closure test. Several checks were carried out to estimate the systematic uncertainty from the shape assumed for the impact-parameter distributions of the prompt and feed-down components. The fit

was repeated fixing the Gaussian width in the F^{prompt} functions to the values expected from the simulation and using template distributions from the simulation in place of the $F^{\text{feed-down}}$ and F^{prompt} functional forms. Furthermore, the stability of the results against a possible imperfect description of the impact-parameter resolution in the simulation was verified with a dedicated "fast" simulation in which the reconstructed track properties were modified to match the impact-parameter resolution measured in data, following the procedure described in Ref. [71]. In addition, the fit procedure was also repeated after tuning the p_{T} distributions of prompt and feed-down D mesons in the simulation to match those predicted by FONLL calculations. The uncertainty deriving from the parametrization of F^{backgr} was estimated by extracting the background impact-parameter distribution from different invariant-mass intervals. Overall, the systematic uncertainty arising from the shape assumed for prompt D-meson, feed-down D-meson, and background impact-parameter distributions is typically smaller than 4%. The systematic effect owing to the uncertainty on the signal and background yields was determined by repeating the fit with S and B varied according to the quadratic sum of the statistical and systematic uncertainties on the raw yield described in Sec. III C. The resulting deviation of the prompt D-meson raw yield, $f_{\text{prompt}}S$, was used to define the related systematic uncertainty, which ranges from 0% to 10% depending on the meson species and p_{T}, with typical values around 2% at intermediate p_{T}. It was also checked that the variation of the width of the invariant-mass (mass difference for D^{*+} mesons) interval around the D-meson peak in which f_{prompt} is evaluated yields a sizable effect (3%) only for D^{*+} mesons. Finally, a Monte Carlo closure test was carried out to verify the consistency of the procedure with simulated data by comparing the f_{prompt} values recovered with the impact-parameter fit and the input ones: The difference, typically about 1%, was considered as a systematic uncertainty. The total systematic uncertainty on f_{prompt} with the data-driven approach is about 2% for D^0 mesons and 5% for D^+ and D^{*+} mesons for $p_{\text{T}} < 12$ GeV/c and increases at higher p_{T} up to 11% for D^{*+} mesons in the interval $16 < p_{\text{T}} < 24$ GeV/c.

The prompt fraction of D^0, D^+, and D^{*+} mesons measured with this method is shown in Fig. 4 (right). For the interval $1 < p_{\text{T}} < 2$ GeV/c, given the poor precision of the impact-parameter fit, a lower limit could be estimated only for D^0 mesons at a 95% confidence level on the basis of statistical and systematic uncertainties. For the same reason, in the highest p_{T} interval, $16 < p_{\text{T}} < 24$ GeV/c, the prompt fraction could be determined with the data-driven method only for D^{*+} mesons. The prompt fraction measured with the impact-parameter fits is found to be compatible with the FONLL-based estimation within uncertainties. For D^0 mesons, the data-driven approach provides a more precise determination of the prompt fraction, while for D^{*+} and D^+ mesons smaller uncertainties are obtained with the FONLL-based method. In addition, the data-driven results are not available at low p_{T} ($p_{\text{T}} < 2$ GeV/c) and, for D^0 and D^+ mesons, at high p_{T} ($p_{\text{T}} > 16$ GeV/c). Finally, it should also be considered that the systematic uncertainty on the FONLL-based f_{prompt} calculation partially cancels in the computation of the nuclear modification factor, because it is correlated between the p-Pb cross section and the pp reference. Note that for the data sample of pp collisions at $\sqrt{s} = 7$ TeV used to compute the reference for the nuclear modification factor, f_{prompt} could be measured with the data-driven method only for D^0 mesons with poor statistical precision in a limited p_{T} interval ($2 < p_{\text{T}} < 12$ GeV/c) [50]. For these reasons, the FONLL-based method was used in the calculation of the production cross sections and nuclear modification factors with the current data samples. The analysis presented here demonstrates that the data-driven method will become fully applicable on the upcoming larger data samples.

IV. D^0 ANALYSIS IN pp AND p-Pb COLLISIONS WITHOUT DECAY-VERTEX RECONSTRUCTION

A. Analysis method

To extend the measurement of D-meson production to $p_{\text{T}} < 1$ GeV/c, a different analysis method, not based on geometrical selections on the displaced decay-vertex topology, was developed for the two-body decay $D^0 \to K^-\pi^+$ (and its charge conjugate). Indeed, at very low p_{T}, the D-meson decay topology cannot be efficiently resolved because of the insufficient resolution of the track impact parameter and the small Lorentz boost. Furthermore, selection criteria based on secondary-vertex displacement tend to select with higher efficiency nonprompt D mesons from beauty-hadron decays, thus increasing the systematic uncertainty on the subtraction of the beauty feed-down contribution. Using an analysis technique mainly based on particle identification and on the estimation and subtraction of the combinatorial background, it was possible to measure the D^0-meson yield down to $p_{\text{T}} = 0$ in pp and p-Pb collisions.

The D^0 yield was extracted in eight p_{T} intervals in the range $0 < p_{\text{T}} < 12$ GeV/c from an invariant-mass analysis of pairs of kaons and pions with opposite charge sign (unlike sign, ULS). D^0 candidates were defined from tracks with $|\eta| < 0.8$ and $p_{\text{T}} > 0.3$ GeV/c (0.4 GeV/c in the p-Pb analysis). Tracks were selected with the same criteria described in Sec. III A for the analysis with decay-vertex reconstruction, with the only difference that the request of at least one hit in either of the two layers of the SPD was not applied for pp collisions. Pion and kaon identification was based on the same strategy used in the analysis with decay-vertex reconstruction, i.e., based on compatibility selections at 3σ level between the measured and expected dE/dx in the TPC and time-of-flight from the interaction vertex to the TOF detector. Tracks without TOF information were identified based only on the TPC dE/dx signal. The resulting D^0 and $\overline{D}^0$ candidates were selected by applying a fiducial acceptance cut $|y_{\text{lab}}| < 0.8$ on their rapidity. As compared to the analysis with decay-vertex reconstruction described in Sec. III A, a wider fiducial acceptance region was used in this analysis to preserve more candidates at low p_{T}. The resulting invariant-mass distributions of $K\pi$ pairs in the transverse momentum intervals $0 < p_{\text{T}} < 1$ GeV/c and $1 < p_{\text{T}} < 2$ GeV/c are shown in the left-hand panels of Figs. 5 and 6 for pp and p-Pb collisions, respectively.

Four different techniques were used to estimate the background distribution: (i) like-sign pairs, (ii) event mixing, (iii) track rotation, and (iv) sideband fit. The like-sign (LS) method is based on $K\pi$ combinations with same charge

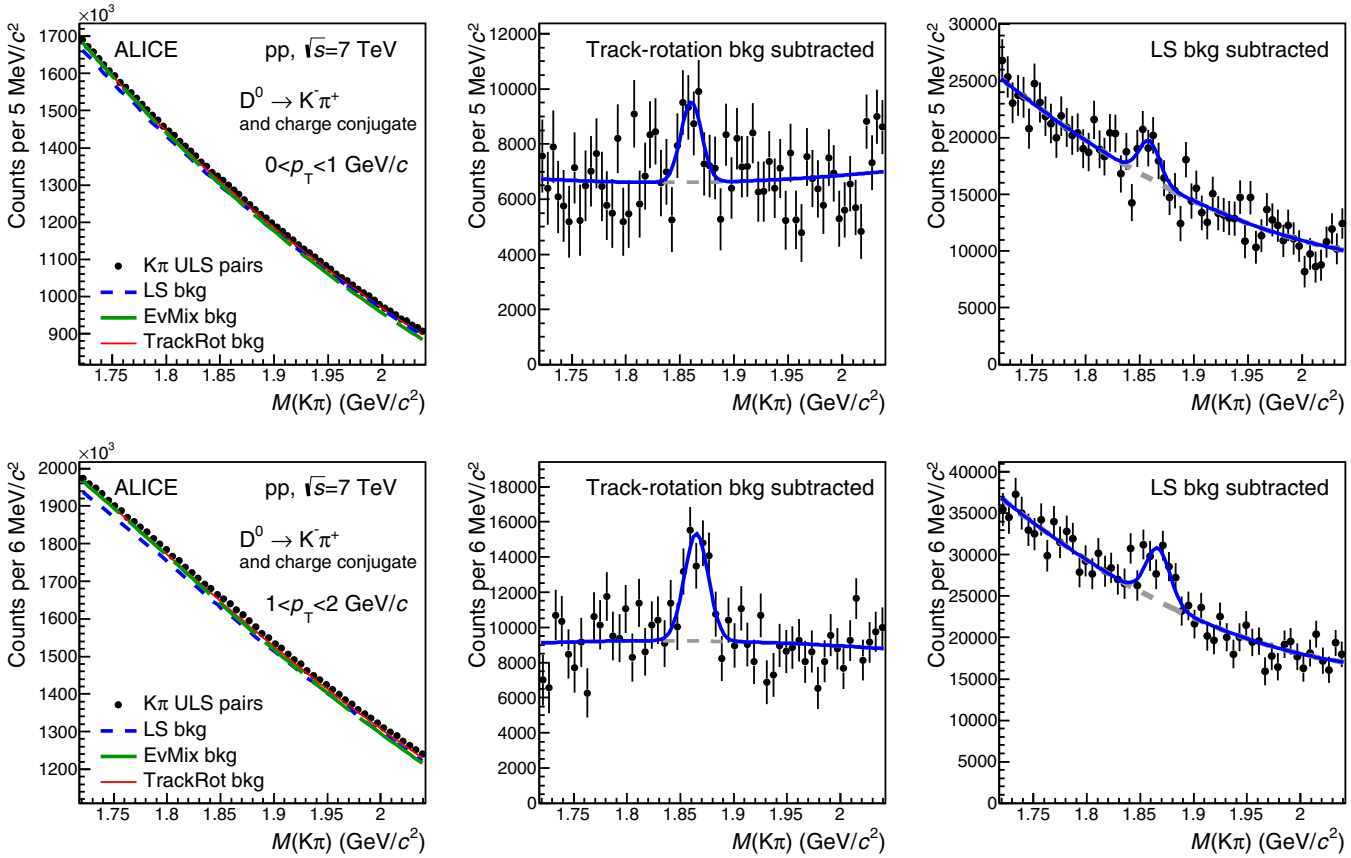

FIG. 5. Invariant-mass distributions of $D^0 \to K^-\pi^+$ candidates (and charge conjugates) in pp collisions at $\sqrt{s} = 7$ TeV for two p_T intervals: $0 < p_T < 1$ GeV/c (top panels) and $1 < p_T < 2$ GeV/c (bottom panels). For both p_T intervals, the left panels display the invariant-mass distribution of all ULS $K\pi$ pairs together with the background distributions estimated with the LS, event-mixing, and track-rotation techniques. The middle and right panels show the invariant-mass distributions after subtraction of the background from the track-rotation and LS techniques. Fit functions are superimposed.

sign. In each p_T interval, the ULS background invariant-mass distribution was estimated from the LS ones as $N_{K^+\pi^-} = 2\sqrt{N_{K^+\pi^+}N_{K^-\pi^-}}$, where $N_{K^+\pi^+}$ and $N_{K^-\pi^-}$ are the number of like-sign $K\pi$ pairs in a given invariant-mass interval. The event-mixing method estimates the uncorrelated background by pairing each kaon of a given event with all pions of other events having similar multiplicity and vertex position along the beam axis. In the track-rotation technique, for each D^0 (and $\overline{D}^0$) candidate, up to nine combinatorial-background-like candidates were created by rotating the kaon track by different angles in the range between $\frac{5\pi}{6}$ and $\frac{7\pi}{6}$ rad in azimuth. In the case of the event-mixing and track-rotation methods, the background is normalized to match the yield of $K\pi$ pairs at one edge of the invariant-mass range considered for the extraction of the D^0 raw yield.

The invariant-mass distributions of background candidates estimated with these three methods (i)–(iii) are shown as lines in the left panels of Figs. 5 and 6 for the pp and p-Pb cases, respectively. The background distribution is subtracted from the ULS $K\pi$ invariant-mass distribution. Some examples of the resulting distributions, which contain the D^0 signal and the remaining background, are shown in Fig. 5 for the track-rotation (middle panels) and LS (right-hand panels) methods in pp interactions and in the middle panels of Fig. 6 for the event-mixing method in p-Pb collisions. The D^0 raw yield (sum of particle and antiparticle contributions) was extracted via a fit to the background-subtracted invariant-mass distribution. The fit function is composed of a Gaussian term to describe the signal and a second-order polynomial function to model the remaining background.

The fourth approach to the background treatment consists of a two-step fit to the ULS $K\pi$ invariant-mass distribution. In the first step, the sidebands of the D^0 peak $[|M(K\pi) - M(D^0)| > 2.5\sigma$, where σ is the Gaussian width of the D^0 peak from the simulation] were used to evaluate the background shape, which was modeled with a fourth-order polynomial for $p_T < 2$ GeV/c and with a second-order polynomial for $p_T > 2$ GeV/c. In the second step, the invariant-mass distribution was fitted in the whole range, using a Gaussian function to model the signal and the polynomial function from the previous step to describe the background. In the right-hand panels of Fig. 6 the invariant-mass distribution of D^0 candidates after subtracting the background estimated from the sidebands is shown, together with the Gaussian function that describes the signal peak.

In the fits for all four methods, the width of the Gaussian was fixed to the value from the simulation, while the centroid was left as a free parameter of the fit and was found to be

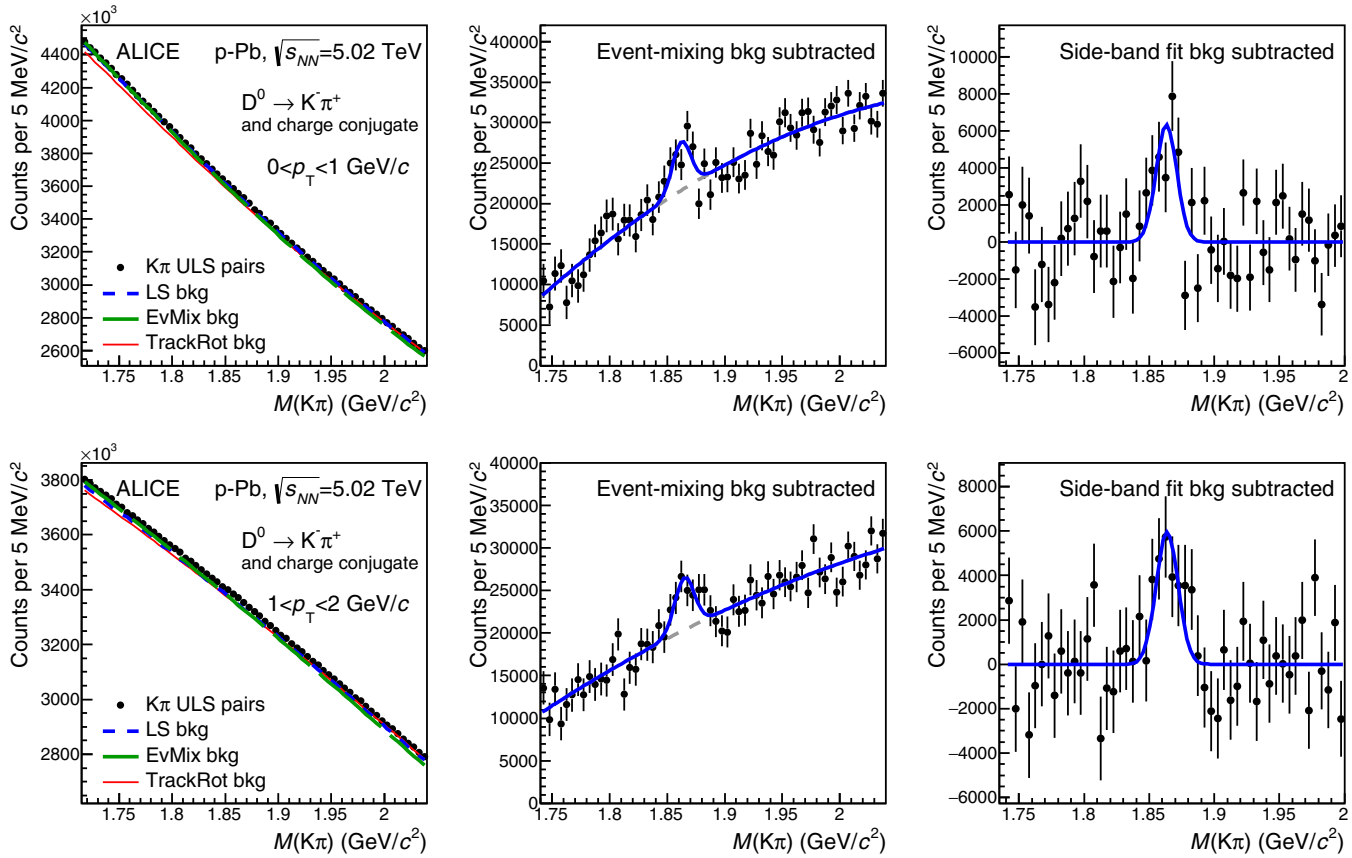

FIG. 6. Invariant-mass distributions of $D^0 \to K^-\pi^+$ candidates (and charge conjugates) in p-Pb collisions at $\sqrt{s_{NN}} = 5.02$ TeV for two p_T intervals: $0 < p_T < 1$ GeV/c (top panels) and $1 < p_T < 2$ GeV/c (bottom panels). For both p_T intervals, the left panels display the invariant-mass distribution of all ULS $K\pi$ pairs together with the background distributions estimated with the LS, event-mixing, and track-rotation techniques. The middle and right panels show the invariant-mass distributions after subtraction of the background from the event-mixing and sideband fit techniques. Fit functions are superimposed.

compatible, within uncertainties, with the PDG world-average value of the D^0 mass [62].

The raw-yield values from the four methods for the background subtraction were found to be consistent within 10% in all p_T intervals of the pp and p-Pb data samples. The arithmetic average of the four values was, therefore, computed and used in the calculation of the cross sections. The statistical uncertainties on these average raw-yield values were defined as the arithmetic average of the uncertainties from the four background-subtraction methods. In the case of the pp sample, the signal-to-background ratio ranges from 10^{-3} (at low p_T) to 2×10^{-2} (at high p_T), while the statistical significance is about 4 in the bin $0 < p_T < 1$ GeV/c and larger than 6 up to $p_T = 4$ GeV/c. For the p-Pb sample, the signal-to-background ratio increases from 7×10^{-4} to 4×10^{-2} with increasing p_T and the statistical significance is about 4 in the two lowest p_T intervals and larger than 7 at higher p_T. The statistical uncertainties on the raw yield are larger than those obtained in the analysis with decay-vertex reconstruction, except for the interval $1 < p_T < 2$ GeV/c in the case of pp collisions. In both pp and p-Pb collisions, this strategy allowed the measurement of the D^0 signal in the interval $0 < p_T < 1$ GeV/c, which was not accessible with the displaced-vertex selection technique.

B. Corrections

The product of the acceptance and the efficiency, Acc $\times\, \varepsilon$, for D^0-meson reconstruction and selection with the approach described in the previous section was determined using Monte Carlo simulations. Events containing prompt and feed-down D-meson signals were simulated using the PYTHIA v6.4.21 event generator [65] with the Perugia-0 tune [66]. In the case of p-Pb collisions, an underlying event generated with HIJING 1.36 [67] was added to obtain a realistic multiplicity distribution. The calculation of the D^0 efficiency was performed utilizing p_T and event-multiplicity-dependent weights, so as to match the D-meson p_T spectra predicted by FONLL calculations and the measured charged-particle multiplicity distributions at midrapidity. The resulting Acc $\times\, \varepsilon$ of prompt D^0 mesons for the p-Pb sample is shown as a function of p_T in Fig. 7 and compared to that for the analysis with decay-vertex reconstruction. The efficiency is higher by a factor of about 20 at low p_T (3 at high p_T) in the case of the analysis that does not make use of selections on the displacement of the D^0 decay point. The p_T dependence of the Acc $\times\, \varepsilon$ is less steep as compared to the analysis with decay-vertex reconstruction. Note that for the analysis without decay-vertex reconstruction the efficiency is almost independent of p_T and the increase

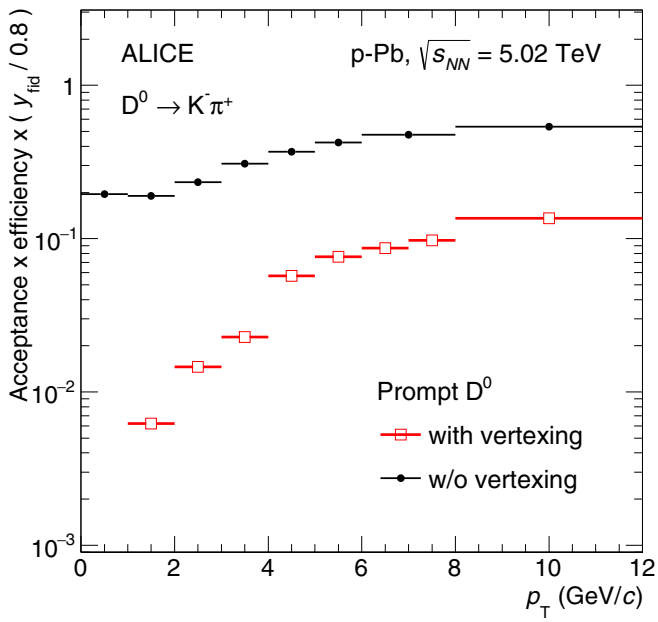

FIG. 7. Product of acceptance and efficiency in p-Pb collisions. The Acc $\times$ ε values from the analysis with decay-vertex reconstruction were rescaled to account for the different fiducial acceptance, $y_{\rm fid}(p_{\rm T})$, selection on the D^0 rapidity.

of the Acc $\times$ ε with increasing $p_{\rm T}$ is mainly determined by the geometrical acceptance of the apparatus, i.e., by the fraction of D^0 mesons with $|y_{\rm lab}| < 0.8$ having the two decay tracks in $|\eta| < 0.8$. Unlike in the analysis with decay-vertex reconstruction, the efficiency is the same for prompt D^0 and for D^0 from beauty-hadron decays, as expected when no selection is made on the displacement of the D^0 decay vertex from the interaction point.

Because the acceptance and the efficiency are the same for prompt and feed-down D^0 mesons, the production cross section for "inclusive" D^0 mesons (i.e., sum of the prompt and feed-down contributions) in the rapidity range $|y_{\rm lab}| < 0.5$ can be calculated as

$$\frac{d^2\sigma^{D^0,\rm incl.}}{dp_{\rm T}dy} = \frac{1}{\Delta p_{\rm T}} \frac{\frac{1}{2}N^{D^0+\overline{D^0},\rm raw}(p_{\rm T})\big|_{|y|<0.8}}{\Delta y} \times \frac{1}{(\rm Acc \times \varepsilon)(p_{\rm T})} \frac{1}{\rm BR L_{int}}. \quad (4)$$

where $N^{D^0+\overline{D^0},\rm raw}(p_{\rm T})$ are the D^0 raw yields.

The production cross section of prompt D^0 mesons was obtained as

$$\frac{d^2\sigma^{D^0,\rm prompt}}{dp_{\rm T}dy} = f_{\rm prompt}(p_{\rm T})\frac{d^2\sigma^{D^0,\rm incl.}}{dp_{\rm T}dy}. \quad (5)$$

The values of $f_{\rm prompt}$ were estimated with the same pQCD-based method used for the analysis with decay-vertex reconstruction as described in Sec. III B. The resulting $f_{\rm prompt}$ values are similar for pp and p-Pb collisions: They decrease with increasing $p_{\rm T}$, from a value of about 0.96 at low $p_{\rm T}$ ($p_{\rm T} < 4$ GeV/c) to about 0.89 in the interval $8 < p_{\rm T} < 12$ GeV/c. The prompt contribution to the D^0-meson raw yield is larger than in the analysis with decay-vertex reconstruction because the feed-down component is not enhanced by the selection criteria.

C. Systematic uncertainties

The following sources of systematic uncertainty were considered for the prompt D^0 cross section: (i) systematic uncertainty owing to the signal extraction from the invariant-mass distributions; (ii) systematic uncertainty affecting the Acc $\times$ ε correction factor; and (iii) systematic uncertainty owing to the beauty feed-down subtraction. In addition, the cross sections are affected by (iv) a global normalization uncertainty, owing to the determination of the integrated luminosity (3.5% in pp and 3.7% in p-Pb) and the $D^0 \to K^-\pi^+$ branching ratio (1.3%).

The systematic uncertainty on the raw-yield extraction was estimated in each $p_{\rm T}$ interval and for each of the four background-subtraction techniques from the distribution of the results obtained by repeating the fit to the invariant-mass distributions varying (i) the fit range and (ii) the functions used to model the signal and background contributions. In particular, an exponential and a third-order polynomial function were used as alternative functional forms to describe the background in the LS, event-mixing, and track-rotation analyses, while in the analysis with the sideband technique polynomials of second, third, and fourth order were used. The signal line shape was varied by using Gaussian functions with the mean fixed to the PDG world-average D^0 mass and varying the widths by $\pm$15% with respect to the value expected from Monte Carlo simulations, based on the deviations between the Gaussian width values observed in data and simulations for the analysis with decay-vertex reconstruction. The effect of the signal line shape was also tested by comparing the raw yields extracted through the fits with those obtained with a method based on the counting of the entries in the invariant-mass distributions after subtraction of the (residual) background estimated from a fit to the sidebands of the D^0 peak. The rms of the distribution of the raw-yield values obtained from the fit variations was assigned as the systematic uncertainty. A possible additional systematic effect could arise from signal candidates that pass the selection criteria also when the (K,π) mass hypothesis for the decay tracks is swapped. A large fraction of these "reflections" is rejected by the applied PID selections. The effect of the remaining contribution was estimated by repeating the fits including an additional term to describe this "reflected-signal" based on its invariant-mass shape in Monte Carlo simulations and was found to be negligible. The reflection contribution induces a smaller systematic effect than in the analysis with decay-vertex reconstruction owing to the smaller signal-to-background ratio. In the case of background estimation with the event-mixing technique, the result was found to be stable against variations of the criteria on vertex position and event multiplicity used to define the samples of collisions to be mixed. The systematic uncertainty was found to be similar for the four different techniques for the background treatment and dominated, in all $p_{\rm T}$ intervals, by the contribution of the signal line shape, which is common to all the background-subtraction approaches. Therefore, when computing the average of LS,

TABLE III. Relative systematic uncertainties on the p_T-differential production cross section of prompt D^0 mesons in p-Pb and pp collisions for the analysis without decay-vertex reconstruction.

	pp				p-Pb			
	p_T interval (GeV/c)				p_T interval (GeV/c)			
	0–1	1–2	2–3	5–6	0–1	1–2	2–3	5–6
Raw yield extraction (%)	14	14	10	14	15	15	10	10
Correction factor								
Tracking efficiency (%)	8	8	8	8	6	6	6	6
Selection efficiency (%)	Negl.	Negl.	Negl.	Negl.	Negl.	Negl.	Negl.	Negl.
PID efficiency (%)	5	5	3	3	Negl.	Negl.	Negl.	Negl.
MC p_T shape (%)	Negl.	Negl.	Negl.	Negl.	Negl.	Negl.	Negl.	Negl.
MC N_{ch} shape (%)	Negl.	Negl.	Negl.	Negl.	Negl.	Negl.	Negl.	Negl.
Feed-down from B (%)	$^{+2}_{-12}$	$^{+2}_{-23}$	$^{+2}_{-10}$	$^{+2}_{-4}$	$^{+2}_{-9}$	$^{+2}_{-17}$	$^{+2}_{-9}$	$^{+2}_{-4}$
Luminosity (%)	3.5				3.7			
Branching ratio (%)	1.3				1.3			

event-mixing, track-rotation, and sideband results, it was propagated as a fully correlated uncertainty.

The uncertainty on the Acc $\times$ ε correction factor originates from imperfections in the detector description in the Monte Carlo simulations, which could affect the particle reconstruction, the D^0-candidate selection efficiency, and the kaon and pion identification. In addition, the correction factor could also be sensitive to the generated shapes of the D^0-meson p_T distribution and of the multiplicity of particles produced in the collision. The systematic uncertainty on the tracking efficiency, which includes the effects of track reconstruction and selection, was estimated by comparing the efficiency of track prolongation from the TPC to the ITS between data and simulation and by varying the track quality selections. It amounts to 4% per track in the pp sample and 3% per track in the p-Pb sample. The stability of the corrected yield was tested against variations of the single-track p_T selection and K/π identification criteria used to form the D^0 candidates. No systematic effect was found to be induced by the single-track p_T cut. In the case of the particle-identification criteria, different selections were tested, and the corrected yields were found to be compatible with those from the standard 3σ cut. Nevertheless, an analysis without applying PID selections could not be performed owing to the insufficient statistical significance of the signal. This test was carried out in the analysis with decay-vertex reconstruction, resulting for the pp sample in an estimated uncertainty of 5% for $p_T < 2$ GeV/c and 3% at higher p_T, while no systematic uncertainty owing to the PID was observed in the p-Pb case. The same uncertainties were therefore assigned to the cross sections obtained with the analysis without decay-vertex reconstruction. The effect on the efficiency owing to possible differences between the real and simulated D^0 momentum and charged-multiplicity distributions was studied by varying the input distributions (using the D-meson p_T shapes predicted by FONLL and PYTHIA and the charged-multiplicity distributions from HIJING and from data) and was found to be negligible.

The systematic uncertainty owing to the subtraction of the beauty-feed-down contribution was estimated following the same procedure of the analysis with decay-vertex reconstruction as described in Sec. III C. As compared to the analysis with decay-vertex reconstruction, the smaller contribution of D^0 from beauty-hadron decays, owing to the absence of a selection on the decay-vertex topology, results in a smaller systematic uncertainty on the feed-down subtraction.

The assigned uncertainties, estimated with the methods described above, are reported in Table III for four p_T intervals and for pp and p-Pb collisions.

V. RESULTS

A. D^0-meson and $c\bar{c}$ production cross section in pp collisions at $\sqrt{s} = 7$ TeV

Figure 8 shows the p_T-differential cross section for D^0 mesons with $|y| < 0.5$ in pp collisions at $\sqrt{s} = 7$ TeV. In the left-hand panel of the figure, the cross section obtained from the analysis without decay-vertex reconstruction is shown for inclusive and for prompt D^0 mesons, i.e., before and after the subtraction of the cross section of D^0 mesons from beauty-hadron decays. The subtraction of the feed-down contribution increases the systematic uncertainties at low p_T, where the uncertainty of the correction is largest, and at high p_T, because the correction increases (f_{prompt} decreases) with p_T. In the right-hand panel of Fig. 8 the cross section for prompt D^0 mesons is compared with that obtained with decay-vertex reconstruction, as published in Ref. [50]. The results are consistent for most of the p_T intervals within one σ of the statistical uncertainties, which are independent for the two measurements because of their very different signal-to-background ratios and efficiencies.

Figure 9 compiles the most precise ALICE measurement of the p_T-differential cross section of prompt D^0 mesons, which uses in each p_T interval the data point with the smallest total uncertainty, namely the results from the analysis without decay-vertex reconstruction in $0 < p_T < 2$ GeV/c and those from the analysis with decay-vertex reconstruction in $2 < p_T < 16$ GeV/c. The cross section is compared with results from perturbative QCD calculations, two of which are based on

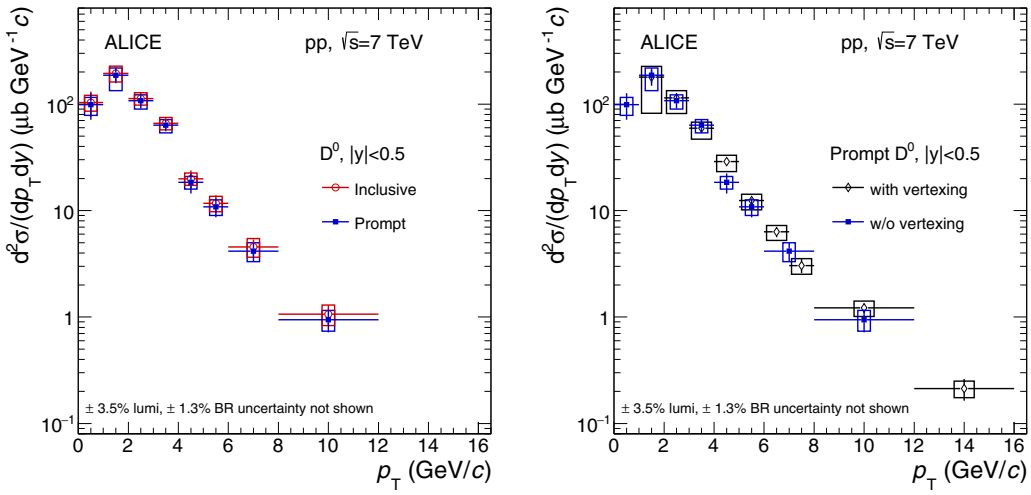

FIG. 8. p_T-differential production cross section of D^0 mesons with $|y| < 0.5$ in pp collisions at $\sqrt{s} = 7$ TeV. (Left) Comparison of prompt and inclusive D^0 mesons (the latter including also D^0 mesons from beauty-hadron decays) from the analysis without decay-vertex reconstruction. (Right) Comparison between the prompt D^0 cross sections measured with [50] and without decay-vertex reconstruction. Here and in all the following figures the symbols are plotted at the center of the p_T intervals (shown by the horizontal lines), the vertical lines represent the statistical uncertainties, and the vertical size of the boxes corresponds to the systematic uncertainties.

collinear factorization (FONLL [5,6][1] and GM-VFNS [2–4]) and one is a leading-order (LO) calculation based on k_T factorization [8]. The ratios of the data to the three calculated cross sections are shown in the bottom-right panel of Fig. 9. The ratio to FONLL is approximately constant at 1.5, but consistent with unity within the theoretical and experimental uncertainties. A ratio data/FONLL larger than unity was observed also at other values of $\sqrt{s}$, from 0.2 to 13 TeV [51,68,73–75]. The ratio to GM-VFNS is approximately constant at 0.75. The ratio to the LO k_T-factorization calculation is consistent with unity for $p_T < 2$ GeV/c and $p_T > 5$ GeV/c, while it is larger than unity for $2 < p_T < 5$ GeV/c.

The average transverse momentum $\langle p_T \rangle$ of prompt D^0 mesons was measured by fitting the cross section reported in Fig. 9 with a power-law function,

$$f(p_T) = C \frac{p_T}{[1 + (p_T/p_0)^2]^n}, \tag{6}$$

where C, p_0, and n are the free parameters. The result is

$$\langle p_T \rangle^{\text{prompt } D^0}_{pp,\,7\,\text{TeV}} = 2.18 \pm 0.08\,(\text{stat.}) \pm 0.07\,(\text{syst.})\ \text{GeV}/c. \tag{7}$$

The systematic uncertainty has three contributions. The first accounts for the uncorrelated systematic uncertainties on the p_T-differential cross section and it was obtained by repeating the fit using the uncorrelated systematic uncertainties as errors on the data points. The second contribution accounts for the uncertainties that are correlated among the p_T intervals and it was computed from the variation of $\langle p_T \rangle$ observed when repeating the fit by moving all data points to the upper (lower) edge of the correlated uncertainties. The third source of systematic uncertainty is attributable to the fit function and it was estimated using different functions and using an alternative method, which is not based on fits to the spectrum, but on direct calculations of $\langle p_T \rangle$ from the data points with different assignments of the average transverse momentum of D^0 mesons in the intervals of the p_T-differential measurement.

The production cross section of prompt D^0 mesons per unit of rapidity at midrapidity was obtained by integrating the p_T-differential cross section shown in Fig. 9. The systematic uncertainty was defined by propagating the yield extraction uncertainties as uncorrelated among p_T intervals (quadratic sum) and all the other uncertainties as correlated (linear sum). The resulting cross section is

$$d\sigma^{\text{prompt } D^0}_{pp,\,7\,\text{TeV}}/dy = 518 \pm 43\,(\text{stat.})^{+\,57}_{-102}\,(\text{syst.}) \pm 18\,(\text{lumi.}) \pm 7\,(\text{BR})\ \mu\text{b}. \tag{8}$$

This measurement is consistent within statistical uncertainties with the value obtained in the analysis with decay-vertex reconstruction [50] [$516 \pm 41\,(\text{stat.})^{+138}_{-179}\,(\text{syst.}) \pm 18\,(\text{lumi.}) \pm 7\,(\text{BR})\ \mu\text{b}$], but it has a total systematic uncertainty reduced by a factor of about two on the low side and almost three on the high side, where the earlier measurement was affected by large uncertainties on the feed-down correction and on the extrapolation to $p_T = 0$ (a factor $1.25^{+0.29}_{-0.09}$ [50]), respectively. For completeness, we also report the inclusive cross section of D^0 mesons, without feed-down subtraction, as obtained by integrating the inclusive cross section shown in Fig. 8 (left):

$$d\sigma^{\text{inclusive } D^0}_{pp,\,7\,\text{TeV}}/dy = 522 \pm 45\,(\text{stat.}) \pm 55\,(\text{syst.}) \pm 18\,(\text{lumi.}) \pm 7\,(\text{BR})\ \mu\text{b}. \tag{9}$$

The central values of the prompt and inclusive $d\sigma/dy$ are numerically very similar. However, this should not lead to a conclusion that the prompt fraction is essentially unity, because the two cross section determinations are to a large extent independent. Indeed, the contribution of D^0 mesons

[1]In the FONLL calculation the $c \to D^0$ fragmentation fraction was updated to the value reported in Ref. [72].

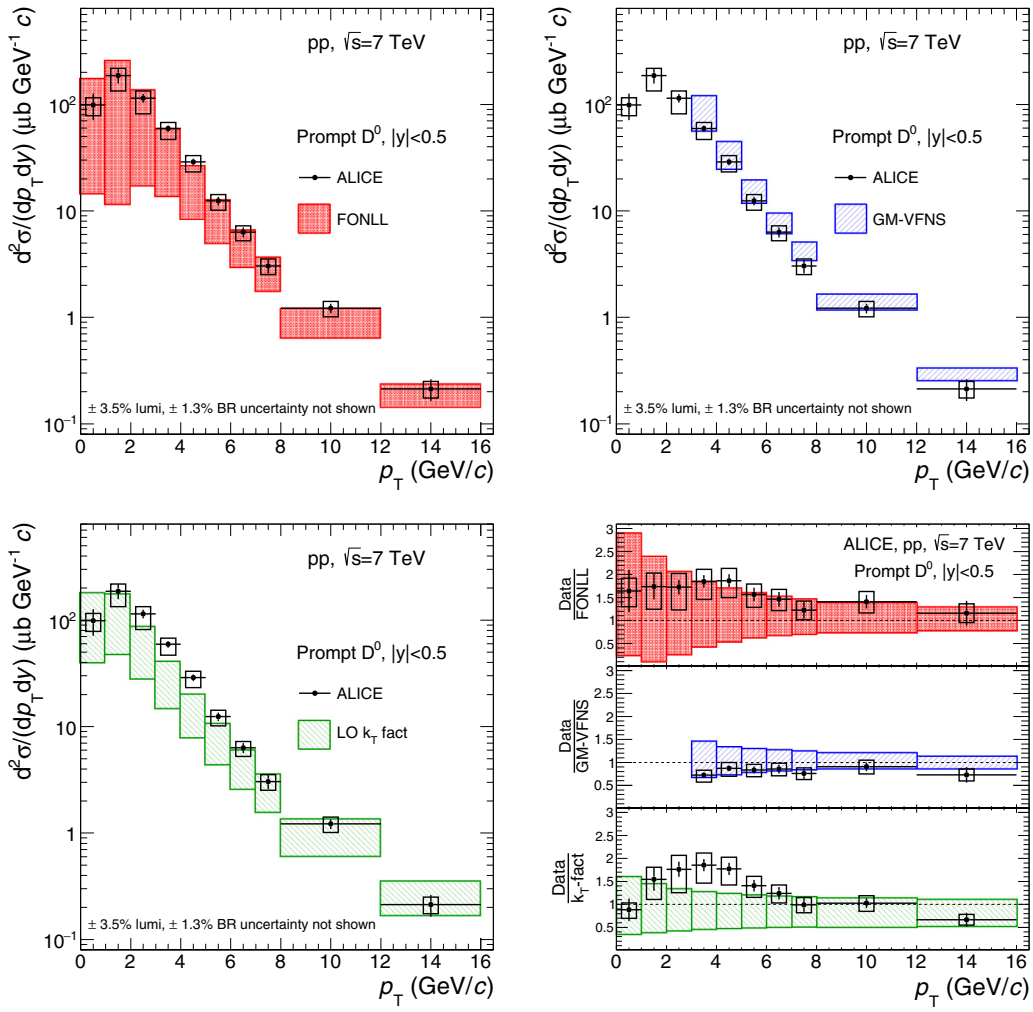

FIG. 9. p_{T}-differential production cross section of prompt D^0 mesons with $|y| < 0.5$ in the interval $0 < p_{\mathrm{T}} < 16$ GeV/c, in pp collisions at $\sqrt{s} = 7$ TeV. The data points in $0 < p_{\mathrm{T}} < 2$ GeV/c are obtained from the analysis described in this article, while the data points in $2 < p_{\mathrm{T}} < 16$ GeV/c are taken from Ref. [50]. The cross section is compared to three pQCD calculations: FONLL [6] (top-left panel), GM-VFNS [4] (top-right panel), and a leading-order (LO) calculation based on k_{T} factorization [8] (bottom-left panel). In the bottom-right panel, the ratios of the data to the three calculated cross sections are reported.

with $p_{\mathrm{T}} > 2$ GeV/c is taken from the results obtained with different analysis techniques in the two cases: The analysis "with decay-vertex reconstruction" is used for the prompt cross section and the analysis "without decay-vertex reconstruction" for the inclusive one. The uncertainties on the results from these two analyses are to a large extent independent, having in common only the 8.5% contribution owing to the tracking and PID efficiency correction, and the contributions from the luminosity and the BR.

The $c\bar{c}$ production cross section per unit of rapidity at midrapidity ($|y| < 0.5$) was calculated by dividing the prompt D^0-meson cross section by the fraction of charm quarks hadronizing into D^0 mesons (fragmentation fraction, FF), 0.542 ± 0.024 [72] and correcting for the different shapes of the distributions of y_{D^0} and $y_{c\bar{c}}$ ($c\bar{c}$ pair rapidity). This correction is composed of two factors. The first factor accounts for the different rapidity shapes of D^0 mesons and single charm quarks and it was evaluated to be unity based on FONLL calculations. A 3% uncertainty on this factor was evaluated from the difference between values from FONLL and the PYTHIA 6 [65] event generator. The second factor is the ratio $d\sigma/dy_{c\bar{c}}/d\sigma/dy_c$, which was estimated from NLO pQCD calculations (MNR [76] and POWHEG [77]) as $\sigma^{c\bar{c}}_{|y|<0.5}/\sigma^{c}_{|y|<0.5} = 1.034$. A 1.5% uncertainty on this factor was estimated from the difference among the values obtained varying the factorization and renormalization scales in the MNR calculation and interfacing, via the POWHEG-BOX package [78], the NLO calculations with a parton shower simulation with PYTHIA. The resulting $c\bar{c}$ cross section per unit of rapidity at midrapidity is

$$d\sigma^{c\bar{c}}_{pp,\,7\,\mathrm{TeV}}/dy = 988 \pm 81\,(\mathrm{stat.})^{+108}_{-195}\,(\mathrm{syst.}) \pm 35\,(\mathrm{lumi.}) \pm 44\,(\mathrm{FF}) \pm 33\,(\mathrm{rap.\ shape})\ \mu\mathrm{b}. \quad (10)$$

The total production cross section of prompt D^0 mesons (average of particles and antiparticles) was calculated by extrapolating to full phase space the cross section measured at midrapidity. The extrapolation factor was defined as the

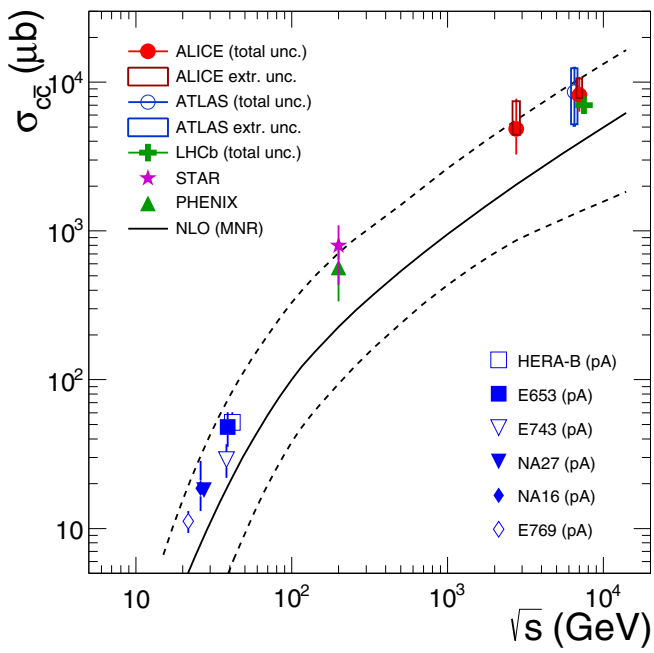

FIG. 10. Total inclusive charm production cross section in nucleon-nucleon collisions as a function of $\sqrt{s}$ [51,68,73,80–82]. Data are from pA collisions for $\sqrt{s} < 100$ GeV and from pp collisions for $\sqrt{s} > 100$ GeV. Data from pA collisions were scaled by $1/A$. Results from NLO pQCD calculations (MNR [76]) and their uncertainties are shown as solid and dashed lines.

ratio of the D^0 production cross sections in full rapidity and in $|y| < 0.5$ calculated with the FONLL central parameters: $8.57^{+2.52}_{-0.38}$. The systematic uncertainty on the extrapolation factor was estimated by considering the contributions owing to (i) the uncertainties on the CTEQ6.6 PDFs [79] and (ii) the variation of the charm-quark mass and the renormalization and factorization scales in the FONLL calculation, as proposed in Ref. [6]. The resulting cross section is

$$\sigma^{\text{prompt } D^0}_{pp,\,7\,\text{TeV}} = 4.43 \pm 0.36\,(\text{stat.})\,^{+0.49}_{-0.88}\,(\text{syst.})\,^{+1.30}_{-0.19}\,(\text{extr.}) \pm 0.16\,(\text{lumi.}) \pm 0.06\,(\text{BR})\ \text{mb}. \quad (11)$$

The total charm production cross section was calculated by dividing the total prompt D^0-meson production cross section by the fragmentation fraction reported above. The resulting $c\bar{c}$ production cross section in pp collisions at $\sqrt{s} = 7$ TeV is

$$\sigma^{c\bar{c}}_{pp,\,7\,\text{TeV}} = 8.18 \pm 0.67\,(\text{stat.})\,^{+0.90}_{-1.62}\,(\text{syst.})\,^{+2.40}_{-0.36}(\text{extr.}) \pm 0.29\,(\text{lumi.}) \pm 0.36\,(\text{FF})\ \text{mb}, \quad (12)$$

which has smaller systematic and extrapolation uncertainties as compared to the value of Ref. [51]. We verified that the precision of the $c\bar{c}$ production cross-section determination does not improve if the results calculated from D^+ and D^{*+} mesons, which have significantly larger extrapolation uncertainties as compared to the D^0 one, are included via a weighted average procedure, as done in Ref. [51]. In Fig. 10, the total charm production cross section is shown as a function of the center-of-mass energy of the collision together with other measurements [51,68,73,80–82]. The LHCb value was computed by multiplying the p_T-integrated charm cross section at forward rapidity [68] by the rapidity extrapolation factor given in Ref. [83]. The proton-nucleus (pA) measurements were scaled by $1/A$, assuming no nuclear effects. The curves show the results of next-to-leading-order pQCD calculations (MNR [76]) together with their uncertainties obtained varying the calculation parameters as suggested in Ref. [6]. The dependence of the charm production cross section on the collision energy is described by the pQCD calculation, with all the data points lying close to the upper edge of the uncertainty band.

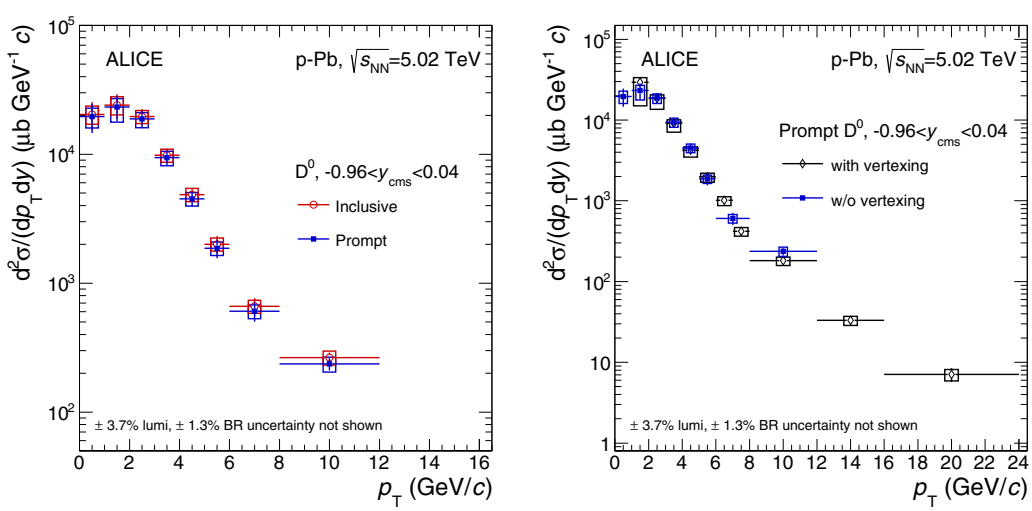

FIG. 11. p_T-differential production cross section of D^0 mesons with $-0.96 < y_{cms} < 0.04$ in p-Pb collisions at $\sqrt{s_{NN}} = 5.02$ TeV. (Left) Comparison of prompt and inclusive D^0 mesons (the latter including also D^0 mesons from beauty-hadron decays) from the analysis without decay-vertex reconstruction. (Right) Comparison between the prompt D^0 cross sections measured with [49] and without decay-vertex reconstruction.

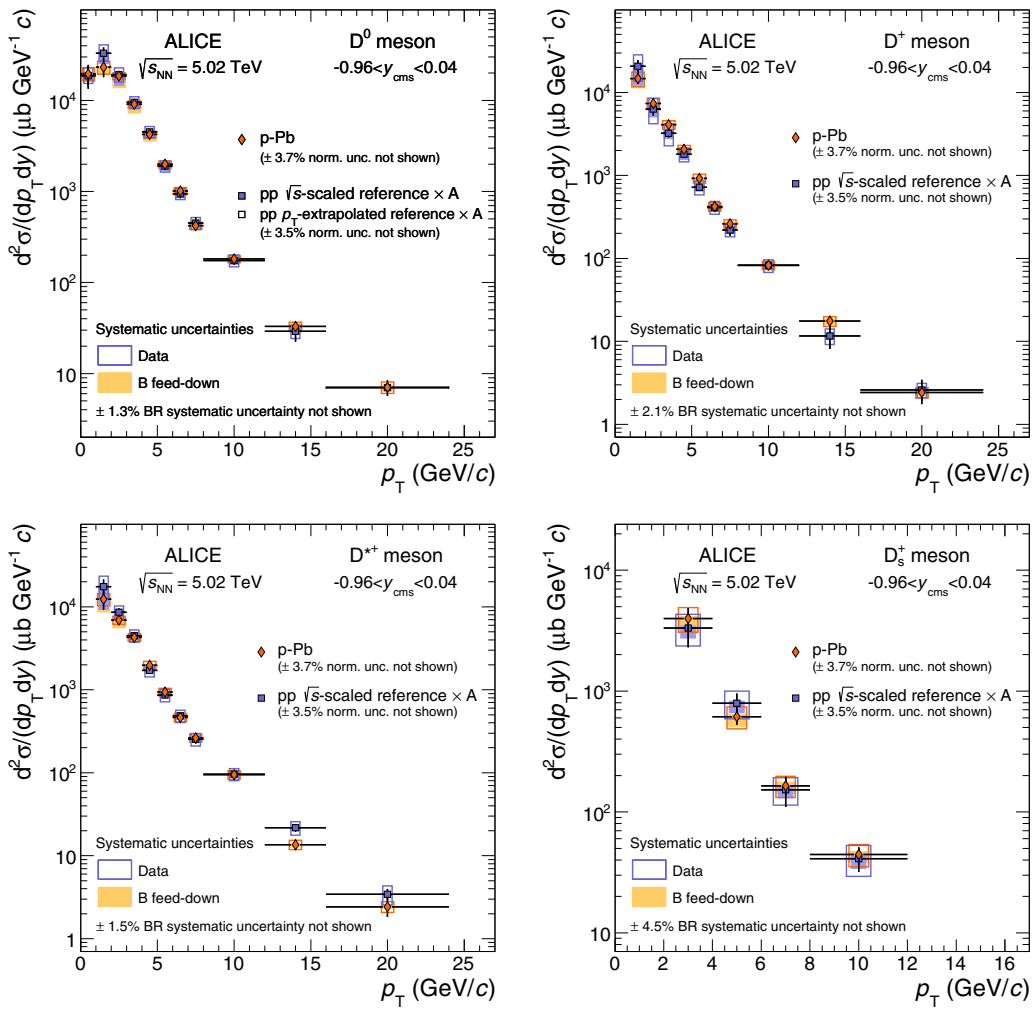

FIG. 12. p_T-differential production cross sections of prompt D^0 (top-left), D^+ (top-right), D^{*+} (bottom-left), and D_s^+ (bottom-right) mesons with $-0.96 < y_{cms} < 0.04$ in p-Pb collisions at $\sqrt{s_{NN}} = 5.02$ TeV, compared with the respective pp reference cross sections scaled by the Pb mass number $A = 208$. For the D^0 meson, the results in $0 < p_T < 2$ GeV/c are obtained from the analysis without decay-vertex reconstruction, while those in $2 < p_T < 24$ GeV/c are taken from the analysis with decay-vertex reconstruction. The results from the other three D-meson species are the same as in Ref. [49]. The systematic uncertainty of the feed-down correction is displayed separately.

B. D-meson production cross section in p-Pb collisions at $\sqrt{s_{NN}} = 5.02$ TeV

Figure 11 shows the p_T-differential production cross section for D^0 mesons with $-0.96 < y_{cms} < 0.04$ in p-Pb collisions at $\sqrt{s_{NN}} = 5.02$ TeV. In the left-hand panel of the figure, the cross section obtained from the analysis without decay-vertex reconstruction is shown for inclusive and for prompt D^0 mesons, while in the right-hand panel the cross section for prompt D^0 mesons is compared with that obtained with decay-vertex reconstruction [49]. The results are consistent within one σ of the statistical uncertainties.

As for pp collisions, the most precise measurement of the prompt D^0 production cross section is obtained using the results of the analysis without decay-vertex reconstruction in the interval $0 < p_T < 2$ GeV/c and those of the analysis with decay-vertex reconstruction for $p_T > 2$ GeV/c [49]. The cross section is shown in the top-left panel of Fig. 12. The total cross section for prompt and inclusive D^0-meson production per unit of rapidity in $-0.96 < y_{cms} < 0.04$ was calculated in the same way as for pp collisions. The resulting values are

$$d\sigma^{\text{prompt } D^0}_{p\text{-Pb, 5.02 TeV}}/dy = 79.0 \pm 7.3\,(\text{stat.})^{+7.1}_{-13.4}\,(\text{syst.}) \pm 2.9\,(\text{lumi.}) \pm 1.0\,(\text{BR})\ \text{mb}, \quad (13)$$

$$d\sigma^{\text{inclusive } D^0}_{p\text{-Pb, 5.02 TeV}}/dy = 83.0 \pm 7.9\,(\text{stat.}) \pm 7.2\,(\text{syst.}) \pm 3.1\,(\text{lumi.}) \pm 1.1\,(\text{BR})\ \text{mb}. \quad (14)$$

The $c\bar{c}$ production cross section in $-0.96 < y_{cms} < 0.04$ is

$$d\sigma^{c\bar{c}}_{p\text{-Pb, 5.02 TeV}}/dy = 151 \pm 14\,(\text{stat.})^{+13}_{-26}\,(\text{syst.}) \pm 6\,(\text{lumi.}) \pm 7\,(\text{FF}) \pm 5\,(\text{rap. shape})\ \text{mb}. \quad (15)$$

The average transverse momentum $\langle p_T \rangle$ of prompt D^0 mesons, obtained with the same procedure described above

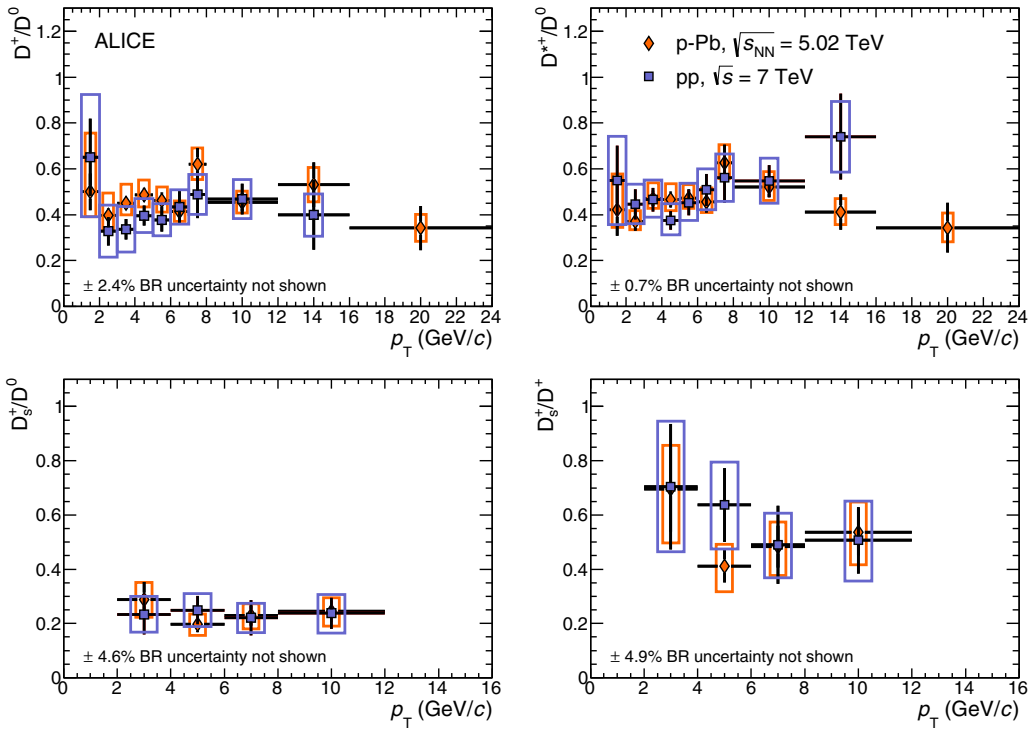

FIG. 13. Ratios of prompt D-meson production cross sections as a function of p_T in pp collisions at $\sqrt{s} = 7$ TeV ($|y_{cms}| < 0.5$) and p-Pb collisions at $\sqrt{s_{NN}} = 5.02$ TeV ($-0.96 < y_{cms} < 0.04$).

for pp collisions, is

$$\langle p_T \rangle^{\text{prompt } D^0}_{p\text{-Pb, 5.02 TeV}} = 2.13 \pm 0.05\,(\text{stat.}) \pm 0.10\,(\text{syst.})\ \text{GeV}/c. \tag{16}$$

The p_T-differential cross sections for the other three D-meson species (D^+, D^{*+}, and D_s^+) [49][2] are shown in the other panels of Fig. 12.

In the same figure, the cross sections in p-Pb collisions are compared with the corresponding pp reference cross sections, scaled by the Pb mass number $A = 208$. The pp reference cross sections at $\sqrt{s} = 5.02$ TeV were obtained by applying a p_T- and D-species-dependent scaling factor to the cross sections measured at $\sqrt{s} = 7$ TeV, namely the cross section shown in Fig. 9 for D^0 mesons and those published in Refs. [50,63] for the other species. The scaling factor was defined as the ratio of the cross sections at 5.02 TeV (in $-0.96 < y_{cms} < 0.04$) and 7 TeV (in $|y_{cms}| < 0.5$) from the FONLL calculation [6], as described in Ref. [85]. Its systematic uncertainty was defined by consistently varying the charm-quark mass and the values of the factorization and renormalization scales at the two energies [85]. The uncertainty decreases with increasing p_T, with values of, for example, $^{+15}_{-5}\%$ for $0 < p_T < 1$ GeV/c, $^{+6}_{-3}\%$ for $3 < p_T < 4$ GeV/c, and $\pm 2\%$ for $p_T > 12$ GeV/c. For D^0 mesons, the cross section was measured in pp collisions at $\sqrt{s} = 7$ TeV up to only $p_T = 16$ GeV/c; the pp reference for the interval $16 < p_T < 24$ GeV/c was defined using the FONLL cross section multiplied by the ratio of data/FONLL in the interval $5 < p_T < 16$ GeV/c, which has a value of about 1.4 (see Ref. [52] for more details).

The ratios of the p_T-differential cross sections of the various D-meson species were calculated taking into account the correlation of the systematic uncertainties induced by the corrections for tracking efficiency and feed-down from beauty decays. In Fig. 13 these ratios are shown together with those for pp collisions at $\sqrt{s} = 7$ TeV (from Ref. [63][3]): Within uncertainties, the relative abundances of the four species are not modified in p-Pb with respect to pp collisions.

Figure 14 shows the cross sections as a function of rapidity for prompt D^0, D^+, and D^{*+} mesons in p-Pb collisions at $\sqrt{s_{NN}} = 5.02$ TeV in three p_T intervals: 2–5 GeV/c (for $-1.16 < y_{cms} < 0.24$) and 5–8 GeV/c and 8–16 GeV/c (for $-1.26 < y_{cms} < 0.34$). The cross sections do not vary with y_{cms}, within uncertainties, for all three p_T intervals. The D^0-meson data are compared with a cross section obtained by multiplying the FONLL [6] result by the mass number A and the nuclear modification factor $R_{p\text{Pb}}$ estimated as a function of y with the MNR NLO pQCD calculation [76] with CTEQ6M PDFs [79] and the EPS09NLO nuclear PDF parametrization [20]. The uncertainty of the calculation is the quadratic sum of the FONLL uncertainty on the cross section

[2]The cross section for D_s^+ mesons in p-Pb collisions and the corresponding pp reference were updated with respect to Ref. [49] to account for the change of the world-average branching ratio of $D_s^+ \to \phi\pi^+ \to K^-K^+\pi^+$ from 2.28% [84] to 2.24% [62].

[3]The ratios involving the D_s^+ meson were updated; see footnote 2.

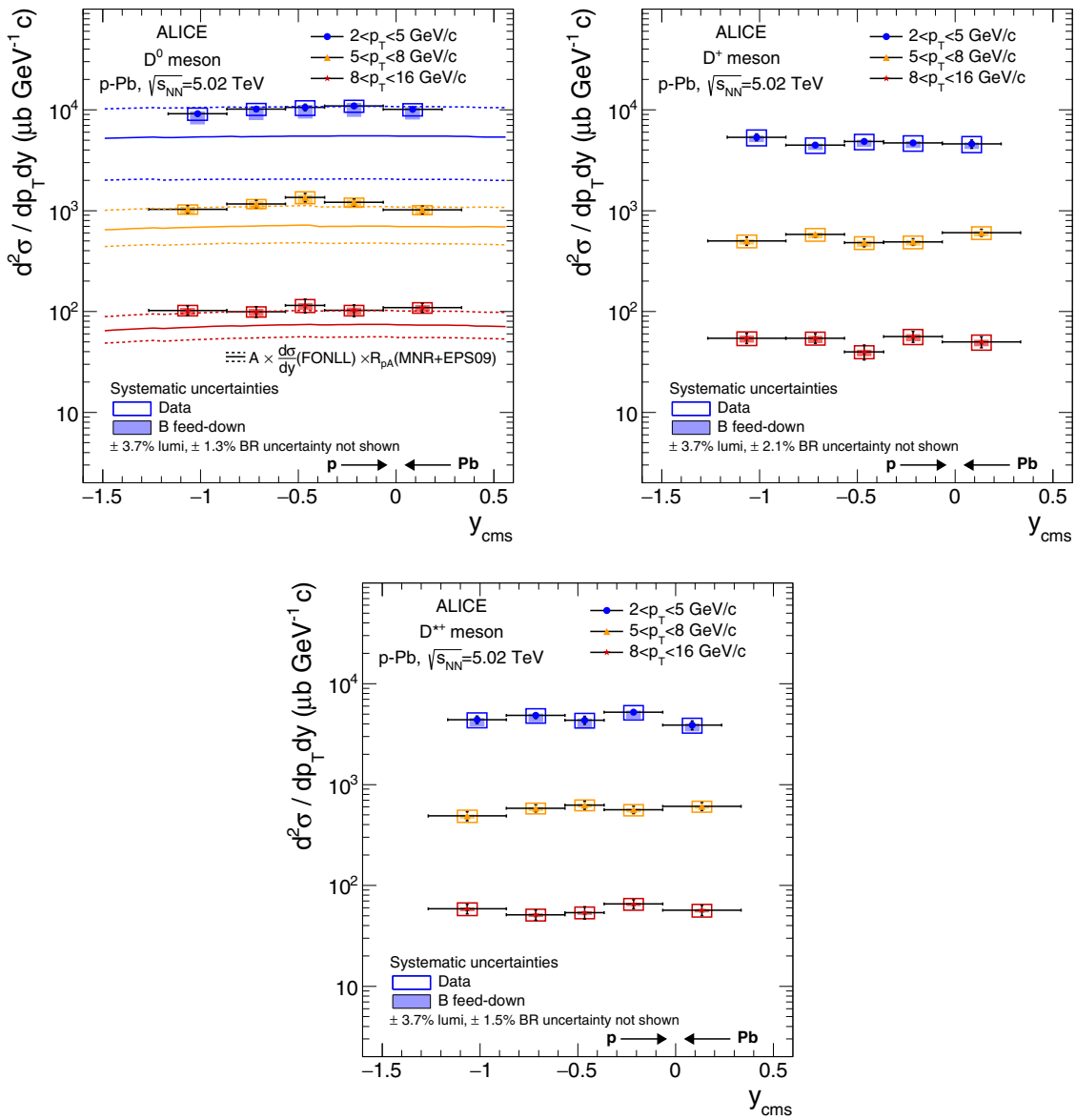

FIG. 14. Production cross sections as a function of rapidity ($y_{\rm cms}$) for prompt D^0, D^+, and D^{*+} mesons in p-Pb collisions at $\sqrt{s_{NN}} =$ 5.02 TeV, for three $p_{\rm T}$ intervals. The D^0-meson data are compared with a cross section obtained by multiplying the FONLL [6] calculation by the mass number A and the nuclear modification factor R_{pA} estimated as a function of y with the MNR NLO pQCD calculation [76], with CTEQ6M PDFs [79], and with the EPS09NLO nuclear PDF parametrization [20].

and the EPS09NLO uncertainty on $R_{p\rm Pb}$. The calculation describes the measurements within uncertainties. As already observed for pp collisions at $\sqrt{s} = 2.76$ and 7 TeV [50,51], the data points lie close to the upper limit of the FONLL uncertainty band. The absence of a visible rapidity dependence in $-1.26 < y_{\rm cms} < 0.34$ is common to the data and the calculation. For the latter, nuclear shadowing induces a cross section variation of only about 2%–3% within this interval.

C. *D*-meson nuclear modification factor in *p*-Pb collisions at $\sqrt{s_{NN}} = 5.02$ TeV

The nuclear modification factor was computed by dividing the $p_{\rm T}$-differential cross section in p-Pb collisions at $\sqrt{s_{NN}} =$ 5.02 TeV by the cross section in pp collisions at the same energy (see Fig. 12) scaled by the lead mass number $A = 208$:

$$R_{p\rm Pb} = \frac{1}{A}\,\frac{d\sigma_{p\rm Pb}^{\rm prompt\,D}/dp_{\rm T}}{d\sigma_{pp}^{\rm prompt\,D}/dp_{\rm T}}. \tag{17}$$

The systematic uncertainties of the p-Pb and pp measurements were considered as independent and propagated quadratically, except for the uncertainty on the feed-down correction, which was recalculated for the ratio of cross sections by consistently varying the FONLL calculation parameters in the numerator and in the denominator.

Figure 15 shows the nuclear modification factors $R_{p\rm Pb}$ of prompt D^0, D^+, and D^{*+} mesons in the left-hand panel and their average, along with the $R_{p\rm Pb}$ of D_s^+ mesons, in the

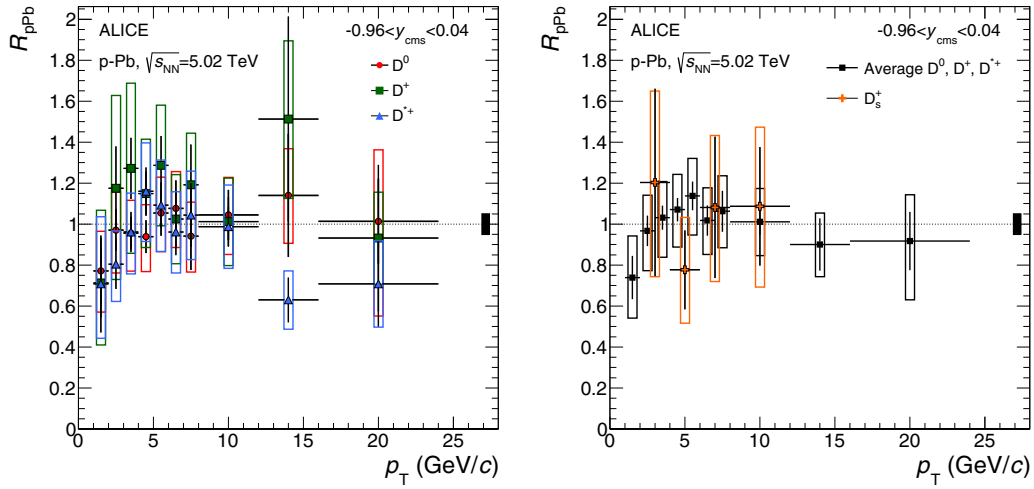

FIG. 15. Nuclear modification factor $R_{p\mathrm{Pb}}$ of prompt D mesons in p-Pb collisions at $\sqrt{s_{NN}} = 5.02$ TeV [49]. (Left) $R_{p\mathrm{Pb}}$ of D^0, D^+, and D^{*+} mesons. (Right) Average $R_{p\mathrm{Pb}}$ of the three nonstrange D-meson species and $R_{p\mathrm{Pb}}$ of D_s^+ mesons. All results are obtained from the analysis with decay-vertex reconstruction.

right-hand panel. All the results are obtained with the analysis based on decay-vertex reconstruction [49]. The average of the nuclear modification factors of the three nonstrange D-meson species was calculated using the inverse of the relative statistical uncertainties as weights. The systematic error of the average was calculated by propagating the uncertainties through the weighted average, where the contributions from tracking efficiency, beauty feed-down correction, and scaling of the pp reference were taken as fully correlated among the three species. $R_{p\mathrm{Pb}}$ is compatible with unity over the full p_{T} interval covered by the measurements and it is also compatible for nonstrange and strange D mesons.

The nuclear modification factor of prompt D^0 mesons in the interval $0 < p_{\mathrm{T}} < 12$ GeV/c was also computed using the cross sections in pp and p-Pb collisions resulting from the analysis without decay-vertex reconstruction. In Fig. 16 it is compared with the result obtained from the analysis with decay-vertex reconstruction, which covers the interval $1 < p_{\mathrm{T}} < 24$ GeV/c [49]. The two measurements are consistent within statistical uncertainties. In the previous sections it was shown that the analysis without decay-vertex reconstruction provides the best determination of the D^0 cross section in the interval $1 < p_{\mathrm{T}} < 2$ GeV/c, where the analysis with decay-vertex reconstruction is affected by a large uncertainty on the feed-down correction. This is not the case for the $R_{p\mathrm{Pb}}$ measurement, because the feed-down uncertainty cancels to a large extent for this observable.

Figure 17 shows the combined measurement of the nuclear modification factor of prompt (nonstrange) D mesons, as obtained by using the D^0 measurement without decay-vertex reconstruction for the interval $0 < p_{\mathrm{T}} < 1$ GeV/c and the average of the measurements for D^0, D^+, and D^{*+} mesons in the interval $1 < p_{\mathrm{T}} < 24$ GeV/c [49]. The data are compared with theoretical results. In the left-hand panel of this figure, four models including only CNM effects are displayed: A calculation based on the color glass condensate formalism [27]; a pQCD calculation based on the MNR formalism [76] with CTEQ6M PDFs [79] and EPS09NLO nuclear modification [20]; a LO pQCD calculation with intrinsic k_{T} broadening, nuclear shadowing, and energy loss of the charm quarks in cold nuclear matter [86]; and a higher-twist calculation based on incoherent multiple scatterings (Kang *et al.*) [87]. The three former calculations describe the data within uncertainties in the entire p_{T} range, while the last one (Kang *et al.*), which has a different trend with respect to the others, is disfavored by the data at $p_{\mathrm{T}} < 3$–4 GeV/c. Cold-nuclear-matter effects are expected to be largest for small p_{T}, where, in addition, the predictions of the different theoretical approaches differ. The uncertainty of the present measurement

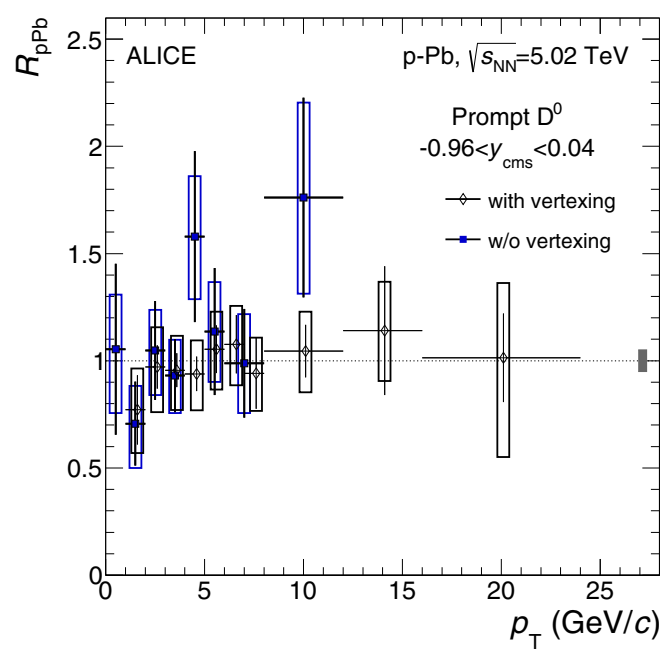

FIG. 16. Comparison of the nuclear modification factors of prompt D^0 mesons as obtained in the analysis with decay-vertex reconstruction [49] and in the analysis without decay-vertex reconstruction.

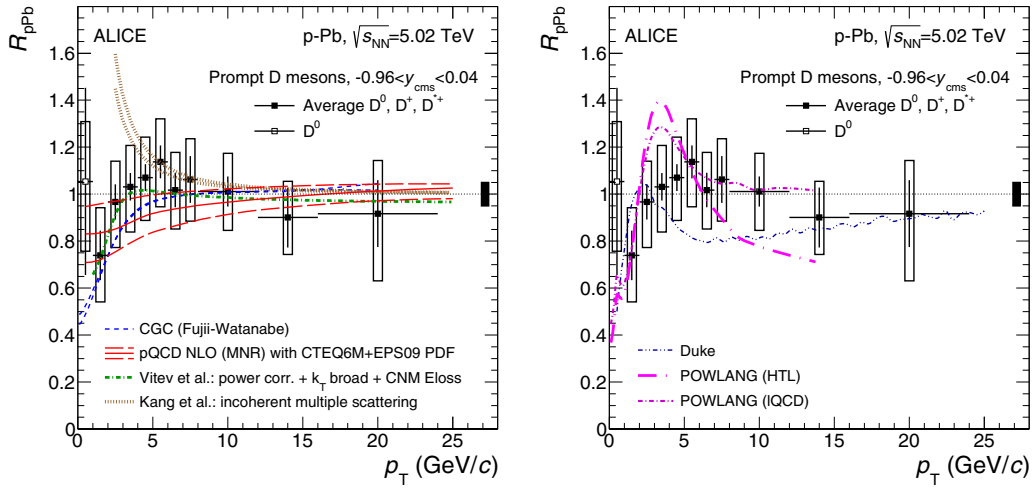

FIG. 17. Nuclear modification factor $R_{p\mathrm{Pb}}$ of prompt D mesons in p-Pb collisions at $\sqrt{s_{NN}} = 5.02$ TeV: average $R_{p\mathrm{Pb}}$ of D^0, D^+, and D^{*+} mesons in the interval $1 < p_{\mathrm{T}} < 24$ GeV/c [49], shown together with the D^0 $R_{p\mathrm{Pb}}$ in $0 < p_{\mathrm{T}} < 1$ GeV/c. In the left-hand panel, the data are compared with results of theoretical calculations including only CNM effects: CGC [27], NLO pQCD [76] with EPS09 nPDFs [20], a LO pQCD calculation with CNM effects (Vitev *et al.*) [86] and a calculation based on incoherent multiple scatterings (Kang *et al.*) [87]. In the right-hand panel, the results of the Duke [47] and POWLANG [48] transport models are compared to the measured D-meson $R_{p\mathrm{Pb}}$.

for the lowest p_{T} interval is about 50% and does not allow us to draw a conclusion. However, the analysis technique without decay-vertex reconstruction, applied on future larger data samples, should provide access to the physics-rich range down to $p_{\mathrm{T}} = 0$. In the right-hand panel of Fig. 17, the data are compared to the results of two transport model calculations, Duke [47] and POWLANG [48], both of them assuming that a quark-gluon plasma is formed in p-Pb collisions. Both models are based on the Langevin approach for the transport of heavy quarks through an expanding deconfined medium described by relativistic viscous hydrodynamics. The Duke model includes both collisional and radiative energy loss. The POWLANG model considers only collisional processes with two choices for the transport coefficients, based on hard-thermal-loop and lattice-QCD (lQCD) calculations, respectively. In both approaches the D-meson nuclear modification factor shows a structure with a maximum at $p_{\mathrm{T}} \approx 2.5$ GeV/c, possibly followed by a moderate (<20%–30%) suppression at higher p_{T}, resulting from the interplay of CNM effects and interactions of charm quarks with the radially expanding medium. The precision of the measured D-meson $R_{p\mathrm{Pb}}$ does not allow us to discriminate between scenarios with only CNM effects or hot medium effects in addition, even though the data seem to disfavor a suppression larger than 15%–20% in the interval $5 < p_{\mathrm{T}} < 10$ GeV/c.

The p_{T}-integrated nuclear modification factor of prompt D^0 mesons in $-0.96 < y_{\mathrm{cms}} < 0.04$ was computed using the $d\sigma^{\mathrm{prompt}\,D^0}/dy$ values for pp and p-Pb collisions reported in Eqs. (8) and (13) and using FONLL to scale the pp cross section to the center-of-mass energy and rapidity interval of the p-Pb measurement. The result is

$$R_{p\mathrm{Pb}}^{\mathrm{prompt}\,D^0}(p_{\mathrm{T}} > 0,\ -0.96 < y_{\mathrm{cms}} < 0.04) = 0.89 \pm 0.11\,(\mathrm{stat.})^{+0.13}_{-0.18}\,(\mathrm{syst.}). \quad (18)$$

VI. SUMMARY

We have presented a comprehensive set of results on charm production in p-Pb and pp collisions, complementing the measurements reported in Refs. [49,50]. The production cross sections of the prompt charmed mesons D^0, D^+, D^{*+}, and D_s^+ in p-Pb collisions at a center-of-mass energy per nucleon pair $\sqrt{s_{NN}} = 5.02$ TeV were measured as a function of p_{T} in the rapidity interval $-0.96 < y_{\mathrm{cms}} < 0.04$. The p_{T}-differential production cross sections, obtained with an analysis method based on the selection of decay topologies displaced from the interaction vertex, were reported in the transverse-momentum range $1 < p_{\mathrm{T}} < 24$ GeV/c for D^0, D^+, and D^{*+} mesons and in the range $2 < p_{\mathrm{T}} < 12$ GeV/c for D_s^+ mesons. The ratios of the cross sections of the four D-meson species were determined as a function of p_{T} and were found to be compatible with those measured in pp collisions at $\sqrt{s} = 7$ TeV in the rapidity interval $|y_{\mathrm{cms}}| < 0.5$.

The production cross sections of the nonstrange D mesons, D^0, D^+, and D^{*+}, were also measured in p-Pb collisions as a function of rapidity in three p_{T} intervals. No significant rapidity dependence was observed in the range $-1.26 < y_{\mathrm{cms}} < 0.34$.

In addition, employing an analysis technique that does not use the reconstruction of the D^0 decay vertex, the prompt D^0 production cross section was measured down to $p_{\mathrm{T}} = 0$ in pp collisions at $\sqrt{s} = 7$ TeV and p-Pb collisions at $\sqrt{s_{NN}} = 5.02$ TeV. The results of the two different analysis techniques, with and without decay-vertex reconstruction, were found to be compatible in the common p_{T} range. The analysis without decay-vertex reconstruction provides a more precise measurement of the D^0 cross section for $p_{\mathrm{T}} < 2$ GeV/c. This allowed a determination of the total (p_{T} integrated) D^0 production cross section, $d\sigma/dy$, at midrapidity, which is not affected by uncertainties owing to the extrapolation

to $p_T = 0$. The resulting cross section in pp collisions at $\sqrt{s} = 7$ TeV is

$$d\sigma^{\text{prompt } D^0}_{pp,\,7\,\text{TeV}}/dy = 518 \pm 43\,(\text{stat.})^{+\,57}_{-102}\,(\text{syst.}) \pm 18\,(\text{lumi.}) \pm 7\,(\text{BR})\ \mu\text{b}.$$

The total systematic uncertainty is smaller by a factor of about two on the low side and almost three on the high side as compared to our previous result [50]. The resulting total $c\bar{c}$ production cross section in pp collisions at $\sqrt{s} = 7$ TeV is

$$\sigma^{c\bar{c}}_{pp\,7\,\text{TeV}} = 8.18 \pm 0.67\,(\text{stat.})\,^{+0.90}_{-1.62}\,(\text{syst.})\,^{+2.40}_{-0.36}(\text{extr.}) \pm 0.29\,(\text{lumi.}) \pm 0.36\,(\text{FF})\ \text{mb}.$$

In p-Pb collisions at $\sqrt{s_{NN}} = 5.02$ TeV, the p_T-integrated prompt-D^0 production cross section at midrapidity ($-0.96 < y_{\text{cms}} < 0.04$) is

$$d\sigma^{\text{prompt } D^0}_{p\text{-Pb},\,5.02\,\text{TeV}}/dy = 79.0 \pm 7.3\,(\text{stat.})^{+\,7.1}_{-13.4}\,(\text{syst.}) \pm 2.9\,(\text{lumi.}) \pm 1.0\,(\text{BR})\ \text{mb}.$$

The p_T-differential nuclear modification factor $R_{p\text{Pb}}$ was found to be compatible with unity in the transverse-momentum interval $0 < p_T < 24$ GeV/c. This result provides clear experimental evidence [49,52] that the modification of the D-meson transverse-momentum distributions observed in Pb-Pb collisions as compared to pp interactions is attributable to final-state effects induced by the interactions of the charm quarks with the hot and dense partonic medium created in ultrarelativistic heavy-ion collisions. The uncertainties of the present measurement are about 20%–30% for $p_T > 1$ GeV/c, considering the average of D^0, D^+, and $D^{*+}R_{p\text{Pb}}$, and about 50% in the interval $0 < p_T < 1$ GeV/c, where the D^0 could be reconstructed with the analysis technique without decay-vertex reconstruction. The results are described within uncertainties by theoretical calculations that include initial-state effects, which are expected to be small for $p_T > 2$ GeV/c but significant for p_T close to 0, where the predictions of the different theoretical approaches differ. The observed $R_{p\text{Pb}}$ is also described by transport calculations assuming the formation of a deconfined medium in p-Pb collisions, even though the data seem to disfavor a suppression larger than 15%–20% in the interval $5 < p_T < 10$ GeV/c. The current precision of the measurement does not allow us to draw conclusions on the role of the different CNM effects and on the possible presence of additional hot-medium effects. However, the analysis technique without decay-vertex reconstruction, applied on future larger data samples, should provide access to the physics-rich range down to $p_T = 0$.

ACKNOWLEDGMENTS

The ALICE Collaboration would like to thank all its engineers and technicians for their invaluable contributions to the construction of the experiment and the CERN accelerator teams for the outstanding performance of the LHC complex. The ALICE Collaboration gratefully acknowledges the resources and support provided by all Grid centres and the Worldwide LHC Computing Grid (WLCG) Collaboration. The ALICE Collaboration acknowledges the following funding agencies for their support in building and running the ALICE detector: State Committee of Science, World Federation of Scientists (WFS), and Swiss Fonds Kidagan, Armenia; Conselho Nacional de Desenvolvimento Científico e Tecnológico (CNPq), Financiadora de Estudos e Projetos (FINEP), Fundação de Amparo à Pesquisa do Estado de São Paulo (FAPESP), Brazil; Ministry of Science & Technology of China (MSTC), National Natural Science Foundation of China (NSFC) and Ministry of Education of China (MOEC); Ministry of Science, Education and Sports of Croatia and Unity through Knowledge Fund, Croatia; Ministry of Education and Youth of the Czech Republic; Danish Natural Science Research Council, the Carlsberg Foundation and the Danish National Research Foundation; The European Research Council under the European Community's Seventh Framework Programme; Helsinki Institute of Physics and the Academy of Finland; French CNRS-IN2P3, the "Région Pays de Loire," "Région Alsace," "Région Auvergne," and CEA, France; German Bundesministerium für Bildung, Wissenschaft, Forschung und Technologie (BMBF) and the Helmholtz Association; General Secretariat for Research and Technology, Ministry of Development, Greece; National Research, Development and Innovation Office (NKFIH), Hungary; Council of Scientific and Industrial Research (CSIR), New Delhi, India; Department of Atomic Energy and Department of Science and Technology of the Government of India; Istituto Nazionale di Fisica Nucleare (INFN) and Centro Fermi-Museo Storico della Fisica e Centro Studi e Ricerche "Enrico Fermi," Italy; Japan Society for the Promotion of Science (JSPS) KAKENHI and MEXT, Japan; National Research Foundation of Korea (NRF); Consejo Nacional de Cienca y Tecnologia (CONACYT), Dirección General de Asuntos del Personal Académico (DGAPA), México; Amérique Latine Formation académique-European Commission (ALFA-EC) and the EPLANET Program (European Particle Physics Latin American Network); Stichting voor Fundamenteel Onderzoek der Materie (FOM) and the Nederlandse Organisatie voor Wetenschappelijk Onderzoek (NWO), Netherlands; Research Council of Norway (NFR); Pontificia Universidad Católica del Perú; National Science Centre, Poland; Ministry of National Education/Institute for Atomic Physics and National Council of Scientific Research in Higher Education (CNCSI-UEFISCDI), Romania; Joint Institute for Nuclear Research, Dubna, Russia, Ministry of Education and Science of Russian Federation, Russian Academy of Sciences, Russian Federal Agency of Atomic Energy, Russian Federal Agency for Science and Innovations and The Russian Foundation for Basic Research; Ministry of Education of Slovakia; Department of Science and Technology, South Africa; Centro de Investigaciones Energéticas, Medioambientales y Tecnológicas (CIEMAT), E-Infrastructure shared between Europe and Latin America (EELA), Ministerio de Economía y Competitividad (MINECO) of Spain, Xunta de Galicia (Consellería de Educación), Centro de Aplicaciones Tecnológicas y Desarrollo Nuclear (CEADEN), Cubaenergía, Cuba, and IAEA (International Atomic Energy Agency); Swedish Research Council (VR) and Knut & Alice Wallenberg Foundation (KAW); National Science and Technology Development Agency (NSDTA), Suranaree University of Technology (SUT), and Office

of the Higher Education Commission under NRU project of Thailand; Ukraine Ministry of Education and Science; United Kingdom Science and Technology Facilities Council (STFC); The United States Department of Energy, the United States National Science Foundation, the State of Texas, and the State of Ohio.

[1] A. Andronic *et al.*, Heavy-flavour and quarkonium production in the LHC era: From proton–proton to heavy-ion collisions, Eur. Phys. J. C **76**, 107 (2016).
[2] B. A. Kniehl, G. Kramer, I. Schienbein, and H. Spiesberger, Inclusive $D^{*\pm}$ production in p anti-p collisions with massive charm quarks, Phys. Rev. D **71**, 014018 (2005).
[3] B. A. Kniehl, G. Kramer, I. Schienbein, and H. Spiesberger, Collinear subtractions in hadroproduction of heavy quarks, Eur. Phys. J. C **41**, 199 (2005).
[4] B. A. Kniehl, G. Kramer, I. Schienbein, and H. Spiesberger, Inclusive charmed-meson production at the CERN LHC, Eur. Phys. J. C **72**, 2082 (2012).
[5] M. Cacciari, M. Greco, and P. Nason, The P(T) spectrum in heavy flavor hadroproduction, J. High Energy Phys. 05 (1998) 007.
[6] M. Cacciari, S. Frixione, N. Houdeau, M. L. Mangano, P. Nason, and G. Ridolfi, Theoretical predictions for charm and bottom production at the LHC, J. High Energy Phys. 10 (2012) 137.
[7] M. Luszczak, R. Maciula, and A. Szczurek, Nonphotonic electrons at RHIC within k(t)-factorization approach and with experimental semileptonic decay functions, Phys. Rev. D **79**, 034009 (2009).
[8] R. Maciula and A. Szczurek, Open charm production at the LHC-k_t-factorization approach, Phys. Rev. D **87**, 094022 (2013).
[9] S. Catani, M. Ciafaloni, and F. Hautmann, High-energy factorization and small x heavy flavor production, Nucl. Phys. B **366**, 135 (1991).
[10] M. Cacciari, M. L. Mangano, and P. Nason, Gluon PDF constraints from the ratio of forward heavy-quark production at the LHC at $\sqrt{S} = 7$ and 13 TeV, Eur. Phys. J. C **75**, 610 (2015).
[11] A. Bhattacharya, R. Enberg, M. H. Reno, I. Sarcevic, and A. Stasto, Perturbative charm production and the prompt atmospheric neutrino flux in light of RHIC and LHC, J. High Energy Phys. 06 (2015) 110.
[12] A. Bhattacharya, R. Enberg, Y. S. Jeong, C. S. Kim, M. H. Reno, I. Sarcevic, and A. Stasto, Prompt atmospheric neutrino fluxes: Perturbative QCD models and nuclear effects, arXiv:1607.00193 [hep-ph].
[13] R. Gauld, J. Rojo, L. Rottoli, and J. Talbert, Charm production in the forward region: Constraints on the small-x gluon and backgrounds for neutrino astronomy, J. High Energy Phys. 11 (2015) 009.
[14] M. V. Garzelli, S. Moch, and G. Sigl, Lepton fluxes from atmospheric charm revisited, J. High Energy Phys. 10 (2015) 115.
[15] A. Andronic, P. Braun-Munzinger, K. Redlich, and J. Stachel, The thermal model on the verge of the ultimate test: Particle production in Pb-Pb collisions at the LHC, J. Phys. G **38**, 124081 (2011).
[16] X. Zhao and R. Rapp, Medium Modifications and Production of Charmonia at LHC, Nucl. Phys. A **859**, 114 (2011).
[17] Y.-p. Liu, Z. Qu, N. Xu, and P.-f. Zhuang, J/psi Transverse Momentum Distribution in High Energy Nuclear Collisions at RHIC, Phys. Lett. B **678**, 72 (2009).
[18] M. Arneodo, Nuclear effects in structure functions, Phys. Rep. **240**, 301 (1994).
[19] S. Malace, D. Gaskell, D. W. Higinbotham, and I. Cloet, The Challenge of the EMC Effect: Existing data and future directions, Int. J. Mod. Phys. E **23**, 1430013 (2014).
[20] K. J. Eskola, H. Paukkunen, and C. A. Salgado, EPS09: A New Generation of NLO and LO Nuclear Parton Distribution Functions, J. High Energy Phys. 04 (2009) 065.
[21] M. Hirai, S. Kumano, and T. H. Nagai, Determination of nuclear parton distribution functions and their uncertainties in next-to-leading order, Phys. Rev. C **76**, 065207 (2007).
[22] D. de Florian and R. Sassot, Nuclear parton distributions at next-to-leading order, Phys. Rev. D **69**, 074028 (2004).
[23] F. Gelis, E. Iancu, J. Jalilian-Marian, and R. Venugopalan, The color glass condensate, Annu. Rev. Nucl. Part. Sci. **60**, 463 (2010).
[24] P. Tribedy and R. Venugopalan, QCD saturation at the LHC: Comparisons of models to p+p and A+A data and predictions for p + Pb collisions, Phys. Lett. B **710**, 125 (2012).
[25] J. L. Albacete, A. Dumitru, H. Fujii, and Y. Nara, CGC predictions for p+Pb collisions at the LHC, Nucl. Phys. A **897**, 1 (2013).
[26] A. H. Rezaeian, CGC predictions for p+A collisions at the LHC and signature of QCD saturation, Phys. Lett. B **718**, 1058 (2013).
[27] H. Fujii and K. Watanabe, Heavy quark pair production in high energy pA collisions: Open heavy flavors, Nucl. Phys. A **920**, 78 (2013).
[28] I. Vitev, Non-Abelian energy loss in cold nuclear matter, Phys. Rev. C **75**, 064906 (2007).
[29] M. Lev and B. Petersson, Nuclear Effects at Large Transverse Momentum in a QCD Parton Model, Z. Phys. C **21**, 155 (1983).
[30] X.-N. Wang, Systematic study of high p_T hadron spectra in pp, p A and A A collisions from SPS to RHIC energies, Phys. Rev. C **61**, 064910 (2000).
[31] B. Z. Kopeliovich, J. Nemchik, A. Schafer, and A. V. Tarasov, Cronin Effect in Hadron Production Off Nuclei, Phys. Rev. Lett. **88**, 232303 (2002).
[32] S. Chatrchyan *et al.* (CMS Collaboration), Observation of long-range near-side angular correlations in proton-lead collisions at the LHC, Phys. Lett. B **718**, 795 (2013).
[33] B. Abelev *et al.* (ALICE Collaboration), Long-range angular correlations on the near and away side in p-Pb collisions at $\sqrt{s_{NN}} = 5.02$ TeV, Phys. Lett. B **719**, 29 (2013).
[34] B. Abelev *et al.* (ALICE Collaboration), Long-range angular correlations of π, K and p in p-Pb collisions at $\sqrt{s_{NN}} = 5.02$ TeV, Phys. Lett. B **726**, 164 (2013).

[35] G. Aad *et al.* (ATLAS Collaboration), Observation of Associated Near-Side and Away-Side Long-Range Correlations in $\sqrt{s_{NN}} = 5.02$ TeV Proton-Lead Collisions with the ATLAS Detector, Phys. Rev. Lett. **110**, 182302 (2013).

[36] J. Adam *et al.* (ALICE Collaboration), Forward-central two-particle correlations in p-Pb collisions at $\sqrt{s_{NN}} = 5.02$ TeV, Phys. Lett. B **753**, 126 (2016).

[37] B. Abelev *et al.* (ALICE Collaboration), Multiplicity dependence of pion, kaon, proton and lambda production in p-Pb collisions at $\sqrt{s_{NN}} = 5.02$ TeV, Phys. Lett. B **728**, 25 (2014).

[38] S. Chatrchyan *et al.* (CMS Collaboration), Study of the production of charged pions, kaons, and protons in pPb collisions at $\sqrt{s_{NN}} = 5.02$ TeV, Eur. Phys. J. C **74**, 2847 (2014).

[39] B. Abelev *et al.* (ALICE Collaboration), Suppression of $\psi(2S)$ production in p-Pb collisions at $\sqrt{s_{NN}} = 5.02$ TeV, J. High Energy Phys. 12 (2014) 073.

[40] R. Aaij *et al.* (LHCb Collaboration), Study of $\psi(2S)$ production and cold nuclear matter effects in pPb collisions at $\sqrt{s_{NN}} = 5$ TeV, J. High Energy Phys. 03 (2016) 133.

[41] J. Adam *et al.* (ALICE Collaboration), Centrality dependence of $\psi(2S)$ suppression in p-Pb collisions at $\sqrt{s_{NN}} = 5.02$ TeV, J. High Energy Phys. 06 (2016) 050.

[42] P. Bozek and W. Broniowski, Correlations from hydrodynamic flow in p-Pb collisions, Phys. Lett. B **718**, 1557 (2013).

[43] P. Bozek and W. Broniowski, Collective dynamics in high-energy proton-nucleus collisions, Phys. Rev. C **88**, 014903 (2013).

[44] K. Dusling and R. Venugopalan, Evidence for BFKL and saturation dynamics from dihadron spectra at the LHC, Phys. Rev. D **87**, 051502 (2013).

[45] L. He, T. Edmonds, Z.-W. Lin, F. Liu, D. Molnar, and F. Wang, Anisotropic parton escape is the dominant source of azimuthal anisotropy in transport models, Phys. Lett. B **753**, 506 (2016).

[46] A. M. Sickles, Possible evidence for radial flow of heavy mesons in d+Au collisions, Phys. Lett. B **731**, 51 (2014).

[47] Y. Xu, S. Cao, M. Nahrgang, W. Ke, G.-Y. Qin, J. Auvinen, and S. A. Bass, Heavy-flavor dynamics in relativistic p-Pb collisions at $\sqrt{s_{NN}} = 5.02$ TeV, Nucl. Part. Phys. Proc. **276–278**, 225 (2016).

[48] A. Beraudo, A. De Pace, M. Monteno, M. Nardi, and F. Prino, Heavy-flavour production in high-energy d-Au and p-Pb collisions, J. High Energy Phys. 03 (2016) 123.

[49] B. Abelev *et al.* (ALICE Collaboration), Measurement of Prompt D-meson Production in p-Pb Collisions at $\sqrt{s_{NN}} = 5.02$ TeV, Phys. Rev. Lett. **113**, 232301 (2014).

[50] B. Abelev *et al.* (ALICE Collaboration), Measurement of charm production at central rapidity in proton-proton collisions at $\sqrt{s} = 7$ TeV, J. High Energy Phys. 01 (2012) 128.

[51] B. Abelev *et al.* (ALICE Collaboration), Measurement of charm production at central rapidity in proton-proton collisions at $\sqrt{s} = 2.76$ TeV, J. High Energy Phys. 07 (2012) 191.

[52] J. Adam *et al.* (ALICE Collaboration), Transverse momentum dependence of D-meson production in Pb-Pb collisions at $\sqrt{s_{NN}} = 2.76$ TeV, J. High Energy Phys. 03 (2016) 081.

[53] K. Aamodt *et al.* (ALICE Collaboration), The ALICE experiment at the CERN LHC, J. Instrum. **3**, S08002 (2008).

[54] B. Abelev *et al.* (ALICE Collaboration), Performance of the ALICE Experiment at the CERN LHC, Int. J. Mod. Phys. A **29**, 1430044 (2014).

[55] K. Aamodt *et al.* (ALICE Collaboration), Alignment of the ALICE Inner Tracking System with cosmic-ray tracks, J. Instrum. **5**, P03003 (2010).

[56] J. Alme *et al.*, The ALICE TPC, a large 3-dimensional tracking device with fast readout for ultra-high multiplicity events, Nucl. Instrum. Methods A **622**, 316 (2010).

[57] A. Akindinov *et al.*, Performance of the ALICE Time-Of-Flight detector at the LHC, Eur. Phys. J. Plus **128**, 44 (2013).

[58] M. Bondila *et al.*, ALICE T0 detector, IEEE Trans. Nucl. Sci. **52**, 1705 (2005).

[59] E. Abbas *et al.* (ALICE Collaboration), Performance of the ALICE VZERO system, J. Instrum. **8**, P10016 (2013).

[60] B. Abelev *et al.* (ALICE Collaboration), Measurement of visible cross sections in proton-lead collisions at $\sqrt{s_{NN}} = 5.02$ TeV in van der Meer scans with the ALICE detector, J. Instrum. **9**, P11003 (2014).

[61] B. Abelev *et al.* (ALICE Collaboration), Measurement of inelastic, single- and double-diffraction cross sections in proton-proton collisions at the LHC with ALICE, Eur. Phys. J. C **73**, 2456 (2013).

[62] K. A. Olive *et al.* (Particle Data Group Collaboration), Review of Particle Physics, Chin. Phys. C **38**, 090001 (2014).

[63] B. Abelev *et al.* (ALICE Collaboration), D_s^+ meson production at central rapidity in proton–proton collisions at $\sqrt{s} = 7$ TeV, Phys. Lett. B **718**, 279 (2012).

[64] J. Adam *et al.* (ALICE Collaboration), Particle identification in ALICE: A Bayesian approach, Eur. Phys. J. Plus **131**, 168 (2016).

[65] T. Sjostrand, S. Mrenna, and P. Z. Skands, PYTHIA6.4 Physics and manual, J. High Energy Phys. 05 (2006) 026.

[66] P. Z. Skands, Tuning Monte Carlo generators: The Perugia tunes, Phys. Rev. D **82**, 074018 (2010).

[67] X.-N. Wang and M. Gyulassy, HIJING: A Monte Carlo model for multiple jet production in pp, pA and AA collisions, Phys. Rev. D **44**, 3501 (1991).

[68] R. Aaij *et al.* (LHCb Collaboration), Prompt charm production in pp collisions at $\sqrt{s} = 7$ TeV, Nucl. Phys. B **871**, 1 (2013).

[69] ALICE Collaboration, Supplemental figures: Measurement of prompt D-meson production in p-Pb collisions at $\sqrt{s_{NN}} = 5.02$ TeV, http://cds.cern.ch/record/2032473.

[70] D. J. Lange, The evtgen particle decay simulation package, Nucl. Instrum. Methods Phys. Res., Sect. A **462**, 152 (2001).

[71] B. Abelev *et al.* (ALICE Collaboration), Conceptual design report for the upgrade of the alice its, Technical Report CERN-LHCC-2012-013, LHCC-P-005, CERN, Geneva, August 2012, http://cds.cern.ch/record/1475244.

[72] L. Gladilin, Fragmentation fractions of c and b quarks into charmed hadrons at LEP, Eur. Phys. J. C **75**, 19 (2015).

[73] L. Adamczyk *et al.* (STAR Collaboration), Measurements of D^0 and D^* production in $p + p$ collisions at $\sqrt{s} = 200$ GeV, Phys. Rev. D **86**, 072013 (2012).

[74] D. Acosta *et al.* (CDF Collaboration), Measurement of Prompt Charm Meson Production Cross Sections in $p\bar{p}$ Collisions at $\sqrt{s} = 1.96$ TeV, Phys. Rev. Lett. **91**, 241804 (2003).

[75] R. Aaij *et al.* (LHCb Collaboration), Measurements of prompt charm production cross-sections in pp collisions at $\sqrt{s} = 13$ TeV, J. High Energy Phys. 03 (2016) 159.

[76] M. L. Mangano, P. Nason, and G. Ridolfi, Heavy quark correlations in hadron collisions at next-to-leading order, Nucl. Phys. B **373**, 295 (1992).

[77] S. Frixione, P. Nason, and G. Ridolfi, A Positive-weight next-to-leading-order Monte Carlo for heavy flavour hadroproduction, J. High Energy Phys. 09 (2007) 126.

[78] S. Alioli, P. Nason, C. Oleari, and E. Re, A general framework for implementing NLO calculations in shower Monte Carlo programs: The POWHEG BOX, J. High Energy Phys. 06 (2010) 043.

[79] J. Pumplin, D. R. Stump, J. Huston, H. L. Lai, P. M. Nadolsky, and W. K. Tung, New generation of parton distributions with uncertainties from global QCD analysis, J. High Energy Phys. 07 (2002) 012.

[80] C. Lourenco and H. K. Wohri, Heavy flavour hadro-production from fixed-target to collider energies, Phys. Rep. **433**, 127 (2006).

[81] A. Adare *et al.* (PHENIX Collaboration), Heavy quark production in $p+p$ and energy loss and flow of heavy quarks in Au+Au collisions at $\sqrt{s_{NN}} = 200$ GeV, Phys. Rev. C **84**, 044905 (2011).

[82] G. Aad *et al.* (ATLAS Collaboration), Measurement of $D^{*\pm}$, $D^{\pm}$ and $D_s^{\pm}$ meson production cross sections in pp collisions at $\sqrt{s} = 7$ TeV with the ATLAS detector, Nucl. Phys. B **907**, 717 (2016).

[83] LHCb Collaboration, Prompt charm production in pp collisions at $\sqrt{s} = 7$ TeV, LHCb-CONF-2010-013, CERN-LHCb-CONF-2010-013.

[84] J. Beringer *et al.* (Particle Data Group Collaboration), Review of Particle Physics (RPP), Phys. Rev. D **86**, 010001 (2012).

[85] R. Averbeck, N. Bastid, Z. C. del Valle, P. Crochet, A. Dainese, and X. Zhang, Reference heavy flavour cross sections in pp Collisions at $\sqrt{s} = 2.76$ TeV, using a pQCD-Driven $\sqrt{s}$-Scaling of ALICE Measurements at $\sqrt{s} = 7$ TeV, arXiv:1107.3243 [hep-ph].

[86] R. Sharma, I. Vitev, and B.-W. Zhang, Light-cone wave function approach to open heavy flavor dynamics in QCD matter, Phys. Rev. C **80**, 054902 (2009).

[87] Z.-B. Kang, I. Vitev, E. Wang, H. Xing, and C. Zhang, Multiple scattering effects on heavy meson production in p+A collisions at backward rapidity, Phys. Lett. B **740**, 23 (2015).

J. Adam,[39] D. Adamová,[85] M. M. Aggarwal,[89] G. Aglieri Rinella,[35] M. Agnello,[96,112] N. Agrawal,[48] Z. Ahammed,[135] S. Ahmad,[19] S. U. Ahn,[69] S. Aiola,[139] A. Akindinov,[59] S. N. Alam,[135] D. S. D. Albuquerque,[123] D. Aleksandrov,[81] B. Alessandro,[112] D. Alexandre,[103] R. Alfaro Molina,[65] A. Alici,[12,106] A. Alkin,[3] J. Alme,[18,37] T. Alt,[42] S. Altinpinar,[18] I. Altsybeev,[134] C. Alves Garcia Prado,[122] C. Andrei,[79] A. Andronic,[99] V. Anguelov,[95] T. Antičić,[100] F. Antinori,[109] P. Antonioli,[106] L. Aphecetche,[115] H. Appelshäuser,[54] S. Arcelli,[27] R. Arnaldi,[112] O. W. Arnold,[36,94] I. C. Arsene,[22] M. Arslandok,[54] B. Audurier,[115] A. Augustinus,[35] R. Averbeck,[99] M. D. Azmi,[19] A. Badalà,[108] Y. W. Baek,[68] S. Bagnasco,[112] R. Bailhache,[54] R. Bala,[92] S. Balasubramanian,[139] A. Baldisseri,[15] R. C. Baral,[62] A. M. Barbano,[26] R. Barbera,[28] F. Barile,[32] G. G. Barnaföldi,[138] L. S. Barnby,[103,35] V. Barret,[71] P. Bartalini,[7] K. Barth,[35] J. Bartke,[119,*] E. Bartsch,[54] M. Basile,[27] N. Bastid,[71] S. Basu,[135] B. Bathen,[55] G. Batigne,[115] A. Batista Camejo,[71] B. Batyunya,[67] P. C. Batzing,[22] I. G. Bearden,[82] H. Beck,[54,95] C. Bedda,[112] N. K. Behera,[51] I. Belikov,[56] F. Bellini,[27] H. Bello Martinez,[2] R. Bellwied,[124] R. Belmont,[137] E. Belmont-Moreno,[65] L. G. E. Beltran,[121] V. Belyaev,[76] G. Bencedi,[138] S. Beole,[26] I. Berceanu,[79] A. Bercuci,[79] Y. Berdnikov,[87] D. Berenyi,[138] R. A. Bertens,[58] D. Berzano,[35] L. Betev,[35] A. Bhasin,[92] I. R. Bhat,[92] A. K. Bhati,[89] B. Bhattacharjee,[44] J. Bhom,[119] L. Bianchi,[124] N. Bianchi,[73] C. Bianchin,[137] J. Bielčík,[39] J. Bielčíková,[85] A. Bilandzic,[82,36,94] G. Biro,[138] R. Biswas,[4] S. Biswas,[4,80] S. Bjelogrlic,[58] J. T. Blair,[120] D. Blau,[81] C. Blume,[54] F. Bock,[75,95] A. Bogdanov,[76] H. Bøggild,[82] L. Boldizsár,[138] M. Bombara,[40] M. Bonora,[35] J. Book,[54] H. Borel,[15] A. Borissov,[98] M. Borri,[126,84] F. Bossú,[66] E. Botta,[26] C. Bourjau,[82] P. Braun-Munzinger,[99] M. Bregant,[122] T. Breitner,[53] T. A. Broker,[54] T. A. Browning,[97] M. Broz,[39] E. J. Brucken,[46] E. Bruna,[112] G. E. Bruno,[32] D. Budnikov,[101] H. Buesching,[54] S. Bufalino,[96,35] P. Buncic,[35] O. Busch,[130] Z. Buthelezi,[66] J. B. Butt,[16] J. T. Buxton,[20] J. Cabala,[117] D. Caffarri,[35] X. Cai,[7] H. Caines,[139] L. Calero Diaz,[73] A. Caliva,[58] E. Calvo Villar,[104] P. Camerini,[25] F. Carena,[35] W. Carena,[35] F. Carnesecchi,[27] J. Castillo Castellanos,[15] A. J. Castro,[127] E. A. R. Casula,[24] C. Ceballos Sanchez,[9] J. Cepila,[39] P. Cerello,[112] J. Cerkala,[117] B. Chang,[125] S. Chapeland,[35] M. Chartier,[126] J. L. Charvet,[15] S. Chattopadhyay,[135] S. Chattopadhyay,[102] A. Chauvin,[94,36] V. Chelnokov,[3] M. Cherney,[88] C. Cheshkov,[132] B. Cheynis,[132] V. Chibante Barroso,[35] D. D. Chinellato,[123] S. Cho,[51] P. Chochula,[35] K. Choi,[98] M. Chojnacki,[82] S. Choudhury,[135] P. Christakoglou,[83] C. H. Christensen,[82] P. Christiansen,[33] T. Chujo,[130] S. U. Chung,[98] C. Cicalo,[107] L. Cifarelli,[12,27] F. Cindolo,[106] J. Cleymans,[91] F. Colamaria,[32] D. Colella,[60,35] A. Collu,[75] M. Colocci,[27] G. Conesa Balbastre,[72] Z. Conesa del Valle,[52] M. E. Connors,[139,†] J. G. Contreras,[39] T. M. Cormier,[86] Y. Corrales Morales,[26,112] I. Cortés Maldonado,[2] P. Cortese,[31] M. R. Cosentino,[122] F. Costa,[35] J. Crkovska,[52] P. Crochet,[71] R. Cruz Albino,[11] E. Cuautle,[64] L. Cunqueiro,[55,35] T. Dahms,[94,36] A. Dainese,[109] M. C. Danisch,[95] A. Danu,[63] D. Das,[102] I. Das,[102] S. Das,[4] A. Dash,[80] S. Dash,[48] S. De,[122] A. De Caro,[12,30] G. de Cataldo,[105] C. de Conti,[122] J. de Cuveland,[42] A. De Falco,[24] D. De Gruttola,[12,30] N. De Marco,[112] S. De Pasquale,[30] R. D. De Souza,[123] A. Deisting,[95,99] A. Deloff,[78] E. Dénes,[138,*] C. Deplano,[83] P. Dhankher,[48] D. Di Bari,[32] A. Di Mauro,[35] P. Di Nezza,[73] B. Di Ruzza,[109] M. A. Diaz Corchero,[10] T. Dietel,[91] P. Dillenseger,[54] R. Divià,[35] Ø. Djuvsland,[18] A. Dobrin,[83,63] D. Domenicis Gimenez,[122] B. Dönigus,[54] O. Dordic,[22] T. Drozhzhova,[54] A. K. Dubey,[135] A. Dubla,[58] L. Ducroux,[132] P. Dupieux,[71] R. J. Ehlers,[139] D. Elia,[105] E. Endress,[104] H. Engel,[53] E. Epple,[139] B. Erazmus,[115] I. Erdemir,[54] F. Erhardt,[131] B. Espagnon,[52] M. Estienne,[115] S. Esumi,[130] J. Eum,[98] D. Evans,[103] S. Evdokimov,[113] G. Eyyubova,[39] L. Fabbietti,[94,36] D. Fabris,[109] J. Faivre,[72] A. Fantoni,[73] M. Fasel,[75] L. Feldkamp,[55] A. Feliciello,[112] G. Feofilov,[134]

J. Ferencei,[85] A. Fernández Téllez,[2] E. G. Ferreiro,[17] A. Ferretti,[26] A. Festanti,[29] V. J. G. Feuillard,[15,71] J. Figiel,[119] M. A. S. Figueredo,[126,122] S. Filchagin,[101] D. Finogeev,[57] F. M. Fionda,[24] E. M. Fiore,[32] M. G. Fleck,[95] M. Floris,[35] S. Foertsch,[66] P. Foka,[99] S. Fokin,[81] E. Fragiacomo,[111] A. Francescon,[35] A. Francisco,[115] U. Frankenfeld,[99] G. G. Fronze,[26] U. Fuchs,[35] C. Furget,[72] A. Furs,[57] M. Fusco Girard,[30] J. J. Gaardhøje,[82] M. Gagliardi,[26] A. M. Gago,[104] K. Gajdosova,[82] M. Gallio,[26] C. D. Galvan,[121] D. R. Gangadharan,[75] P. Ganoti,[90] C. Gao,[7] C. Garabatos,[99] E. Garcia-Solis,[13] C. Gargiulo,[35] P. Gasik,[94,36] E. F. Gauger,[120] M. Germain,[115] M. Gheata,[35,63] P. Ghosh,[135] S. K. Ghosh,[4] P. Gianotti,[73] P. Giubellino,[112,35] P. Giubilato,[29] E. Gladysz-Dziadus,[119] P. Glässel,[95] D. M. Goméz Coral,[65] A. Gomez Ramirez,[53] A. S. Gonzalez,[35] V. Gonzalez,[10] P. González-Zamora,[10] S. Gorbunov,[42] L. Görlich,[119] S. Gotovac,[118] V. Grabski,[65] O. A. Grachov,[139] L. K. Graczykowski,[136] K. L. Graham,[103] A. Grelli,[58] A. Grigoras,[35] C. Grigoras,[35] V. Grigoriev,[76] A. Grigoryan,[1] S. Grigoryan,[67] B. Grinyov,[3] N. Grion,[111] J. M. Gronefeld,[99] F. Grosa,[26] J. F. Grosse-Oetringhaus,[35] R. Grosso,[99] L. Gruber,[114] F. Guber,[57] R. Guernane,[72] B. Guerzoni,[27] K. Gulbrandsen,[82] T. Gunji,[129] A. Gupta,[92] R. Gupta,[92] R. Haake,[55,35] C. Hadjidakis,[52] M. Haiduc,[63] H. Hamagaki,[129] G. Hamar,[138] J. C. Hamon,[56] J. W. Harris,[139] A. Harton,[13] D. Hatzifotiadou,[106] S. Hayashi,[129] S. T. Heckel,[54] E. Hellbär,[54] H. Helstrup,[37] A. Herghelegiu,[79] G. Herrera Corral,[11] B. A. Hess,[34] K. F. Hetland,[37] H. Hillemanns,[35] B. Hippolyte,[56] D. Horak,[39] R. Hosokawa,[130] P. Hristov,[35] C. Hughes,[127] T. J. Humanic,[20] N. Hussain,[44] T. Hussain,[19] D. Hutter,[42] D. S. Hwang,[21] R. Ilkaev,[101] M. Inaba,[130] E. Incani,[24] M. Ippolitov,[76,81] M. Irfan,[19] V. Isakov,[57] M. Ivanov,[99,35] V. Ivanov,[87] V. Izucheev,[113] B. Jacak,[75] N. Jacazio,[27] P. M. Jacobs,[75] M. B. Jadhav,[48] S. Jadlovska,[117] J. Jadlovsky,[117,60] C. Jahnke,[122] M. J. Jakubowska,[136] M. A. Janik,[136] P. H. S. Y. Jayarathna,[124] C. Jena,[29] S. Jena,[124] R. T. Jimenez Bustamante,[99] P. G. Jones,[103] A. Jusko,[103] P. Kalinak,[60] A. Kalweit,[35] J. H. Kang,[140] V. Kaplin,[76] S. Kar,[135] A. Karasu Uysal,[70] O. Karavichev,[57] T. Karavicheva,[57] L. Karayan,[95,99] E. Karpechev,[57] U. Kebschull,[53] R. Keidel,[141] D. L. D. Keijdener,[58] M. Keil,[35] M. Mohisin Khan,[19,‡] P. Khan,[102] S. A. Khan,[135] A. Khanzadeev,[87] Y. Kharlov,[113] A. Khatun,[19] B. Kileng,[37] D. W. Kim,[43] D. J. Kim,[125] D. Kim,[140] H. Kim,[140] J. S. Kim,[43] J. Kim,[95] M. Kim,[140] S. Kim,[21] T. Kim,[140] S. Kirsch,[42] I. Kisel,[42] S. Kiselev,[59] A. Kisiel,[136] G. Kiss,[138] J. L. Klay,[6] C. Klein,[54] J. Klein,[35] C. Klein-Bösing,[55] S. Klewin,[95] A. Kluge,[35] M. L. Knichel,[95] A. G. Knospe,[120,124] C. Kobdaj,[116] M. Kofarago,[35] T. Kollegger,[99] A. Kolojvari,[134] V. Kondratiev,[134] N. Kondratyeva,[76] E. Kondratyuk,[113] A. Konevskikh,[57] M. Kopcik,[117] M. Kour,[92] C. Kouzinopoulos,[35] O. Kovalenko,[78] V. Kovalenko,[134] M. Kowalski,[119] G. Koyithatta Meethaleveedu,[48] I. Králik,[60] A. Kravčáková,[40] M. Krivda,[60,103] F. Krizek,[85] E. Kryshen,[87,35] M. Krzewicki,[42] A. M. Kubera,[20] V. Kučera,[85] C. Kuhn,[56] P. G. Kuijer,[83] A. Kumar,[92] J. Kumar,[48] L. Kumar,[89] S. Kumar,[48] P. Kurashvili,[78] A. Kurepin,[57] A. B. Kurepin,[57] A. Kuryakin,[101] M. J. Kweon,[51] Y. Kwon,[140] S. L. La Pointe,[42,112] P. La Rocca,[28] P. Ladron de Guevara,[11] C. Lagana Fernandes,[122] I. Lakomov,[35] R. Langoy,[41] K. Lapidus,[36,139] C. Lara,[53] A. Lardeux,[15] A. Lattuca,[26] E. Laudi,[35] R. Lea,[25] L. Leardini,[95] S. Lee,[140] F. Lehas,[83] S. Lehner,[114] R. C. Lemmon,[84] V. Lenti,[105] E. Leogrande,[58] I. León Monzón,[121] H. León Vargas,[65] M. Leoncino,[26] P. Lévai,[138] S. Li,[7,71] X. Li,[14] J. Lien,[41] R. Lietava,[103] S. Lindal,[22] V. Lindenstruth,[42] C. Lippmann,[99] M. A. Lisa,[20] H. M. Ljunggren,[33] D. F. Lodato,[58] P. I. Loenne,[18] V. Loginov,[76] C. Loizides,[75] X. Lopez,[71] E. López Torres,[9] A. Lowe,[138] P. Luettig,[54] M. Lunardon,[29] G. Luparello,[25] M. Lupi,[35] T. H. Lutz,[139] A. Maevskaya,[57] M. Mager,[35] S. Mahajan,[92] S. M. Mahmood,[22] A. Maire,[56] R. D. Majka,[139] M. Malaev,[87] I. Maldonado Cervantes,[64] L. Malinina,[67,§] D. Mal'Kevich,[59] P. Malzacher,[99] A. Mamonov,[101] V. Manko,[81] F. Manso,[71] V. Manzari,[35,105] Y. Mao,[7] M. Marchisone,[66,128,26] J. Mareš,[61] G. V. Margagliotti,[25] A. Margotti,[106] J. Margutti,[58] A. Marín,[99] C. Markert,[120] M. Marquard,[54] N. A. Martin,[99] P. Martinengo,[35] M. I. Martínez,[2] G. Martínez García,[115] M. Martinez Pedreira,[35] A. Mas,[122] S. Masciocchi,[99] M. Masera,[26] A. Masoni,[107] A. Mastroserio,[32] A. Matyja,[119] C. Mayer,[119] J. Mazer,[127] M. A. Mazzoni,[110] D. Mcdonald,[124] F. Meddi,[23] Y. Melikyan,[76] A. Menchaca-Rocha,[65] E. Meninno,[30] J. Mercado Pérez,[95] M. Meres,[38] S. Mhlanga,[91] Y. Miake,[130] M. M. Mieskolainen,[46] K. Mikhaylov,[59,67] L. Milano,[75,35] J. Milosevic,[22] A. Mischke,[58] A. N. Mishra,[49] D. Miśkowiec,[99] J. Mitra,[135] C. M. Mitu,[63] N. Mohammadi,[58] B. Mohanty,[80] C. Mohler,[95] L. Molnar,[56] L. Montaño Zetina,[11] E. Montes,[10] D. A. Moreira De Godoy,[55] L. A. P. Moreno,[2] S. Moretto,[29] A. Morreale,[115] A. Morsch,[35] V. Muccifora,[73] E. Mudnic,[118] D. Mühlheim,[55] S. Muhuri,[135] M. Mukherjee,[135] J. D. Mulligan,[139] M. G. Munhoz,[122] K. Münning,[45] R. H. Munzer,[94,36,54] H. Murakami,[129] S. Murray,[66] L. Musa,[35] J. Musinsky,[60] B. Naik,[48] R. Nair,[78] B. K. Nandi,[48] R. Nania,[106] E. Nappi,[105] M. U. Naru,[16] H. Natal da Luz,[122] C. Nattrass,[127] S. R. Navarro,[2] K. Nayak,[80] R. Nayak,[48] T. K. Nayak,[135] S. Nazarenko,[101] A. Nedosekin,[59] R. A. Negrao De Oliveira,[35] L. Nellen,[64] F. Ng,[124] M. Nicassio,[99] M. Niculescu,[63] J. Niedziela,[35] B. S. Nielsen,[82] S. Nikolaev,[81] S. Nikulin,[81] V. Nikulin,[87] F. Noferini,[106,12] P. Nomokonov,[67] G. Nooren,[58] J. C. C. Noris,[2] J. Norman,[126] A. Nyanin,[81] J. Nystrand,[18] H. Oeschler,[95] S. Oh,[139] S. K. Oh,[68] A. Ohlson,[35] A. Okatan,[70] T. Okubo,[47] J. Oleniacz,[136] A. C. Oliveira Da Silva,[122] M. H. Oliver,[139] J. Onderwaater,[99] C. Oppedisano,[112] R. Orava,[46] M. Oravec,[117] A. Ortiz Velasquez,[64] A. Oskarsson,[33] J. Otwinowski,[119] K. Oyama,[95,77] M. Ozdemir,[54] Y. Pachmayer,[95] D. Pagano,[133] P. Pagano,[30] G. Paić,[64] S. K. Pal,[135] P. Palni,[7] J. Pan,[137] A. K. Pandey,[48] V. Papikyan,[1] G. S. Pappalardo,[108] P. Pareek,[49] W. J. Park,[99] S. Parmar,[89] A. Passfeld,[55] V. Paticchio,[105] R. N. Patra,[135] B. Paul,[112] H. Pei,[7] T. Peitzmann,[58] X. Peng,[7] H. Pereira Da Costa,[15] D. Peresunko,[81,76] E. Perez Lezama,[54] V. Peskov,[54] Y. Pestov,[5] V. Petráček,[39] V. Petrov,[113] M. Petrovici,[79] C. Petta,[28] S. Piano,[111] M. Pikna,[38] P. Pillot,[115] L. O. D. L. Pimentel,[82] O. Pinazza,[106,35] L. Pinsky,[124] D. B. Piyarathna,[124] M. Płoskoń,[75] M. Planinic,[131] J. Pluta,[136] S. Pochybova,[138] P. L. M. Podesta-Lerma,[121] M. G. Poghosyan,[86] B. Polichtchouk,[113] N. Poljak,[131] W. Poonsawat,[116] A. Pop,[79] H. Poppenborg,[55] S. Porteboeuf-Houssais,[71] J. Porter,[75] J. Pospisil,[85] S. K. Prasad,[4] R. Preghenella,[106,35] F. Prino,[112] C. A. Pruneau,[137] I. Pshenichnov,[57] M. Puccio,[26] G. Puddu,[24] P. Pujahari,[137] V. Punin,[101] J. Putschke,[137] H. Qvigstad,[22] A. Rachevski,[111] S. Raha,[4] S. Rajput,[92] J. Rak,[125] A. Rakotozafindrabe,[15] L. Ramello,[31] F. Rami,[56] R. Raniwala,[93]

S. Raniwala,[93] S.S. Räsänen,[46] B. T. Rascanu,[54] D. Rathee,[89] I. Ravasenga,[26] K. F. Read,[127,86] K. Redlich,[78] R. J. Reed,[137] A. Rehman,[18] P. Reichelt,[54] F. Reidt,[35,95] X. Ren,[7] R. Renfordt,[54] A. R. Reolon,[73] A. Reshetin,[57] K. Reygers,[95] V. Riabov,[87] R. A. Ricci,[74] T. Richert,[33] M. Richter,[22] P. Riedler,[35] W. Riegler,[35] F. Riggi,[28] C. Ristea,[63] M. Rodríguez Cahuantzi,[2] A. Rodriguez Manso,[83] K. Røed,[22] E. Rogochaya,[67] D. Rohr,[42] D. Röhrich,[18] F. Ronchetti,[35,73] L. Ronflette,[115] P. Rosnet,[71] A. Rossi,[29] F. Roukoutakis,[90] A. Roy,[49] C. Roy,[56] P. Roy,[102] A. J. Rubio Montero,[10] R. Rui,[25] R. Russo,[26] E. Ryabinkin,[81] Y. Ryabov,[87] A. Rybicki,[119] S. Saarinen,[46] S. Sadhu,[135] S. Sadovsky,[113] K. Šafařík,[35] B. Sahlmuller,[54] P. Sahoo,[49] R. Sahoo,[49] S. Sahoo,[62] P. K. Sahu,[62] J. Saini,[135] S. Sakai,[73] M. A. Saleh,[137] J. Salzwedel,[20] S. Sambyal,[92] V. Samsonov,[87,76] L. Šándor,[60] A. Sandoval,[65] M. Sano,[130] D. Sarkar,[135] N. Sarkar,[135] P. Sarma,[44] E. Scapparone,[106] F. Scarlassara,[29] C. Schiaua,[79] R. Schicker,[95] C. Schmidt,[99] H. R. Schmidt,[34] M. Schmidt,[34] S. Schuchmann,[54,95] J. Schukraft,[35] Y. Schutz,[35,115] K. Schwarz,[99] K. Schweda,[99] G. Scioli,[27] E. Scomparin,[112] R. Scott,[127] M. Šefčík,[40] J. E. Seger,[88] Y. Sekiguchi,[129] D. Sekihata,[47] I. Selyuzhenkov,[99] K. Senosi,[66] S. Senyukov,[3,35] E. Serradilla,[10,65] A. Sevcenco,[63] A. Shabanov,[57] A. Shabetai,[115] O. Shadura,[3] R. Shahoyan,[35] A. Shangaraev,[113] A. Sharma,[92] M. Sharma,[92] M. Sharma,[92] N. Sharma,[127] A. I. Sheikh,[135] K. Shigaki,[47] Q. Shou,[7] K. Shtejer,[9,26] Y. Sibiriak,[81] S. Siddhanta,[107] K. M. Sielewicz,[35] T. Siemiarczuk,[78] D. Silvermyr,[33] C. Silvestre,[72] G. Simatovic,[131] G. Simonetti,[35] R. Singaraju,[135] R. Singh,[80] V. Singhal,[135] T. Sinha,[102] B. Sitar,[38] M. Sitta,[31] T. B. Skaali,[22] M. Slupecki,[125] N. Smirnov,[139] R. J. M. Snellings,[58] T. W. Snellman,[125] J. Song,[98] M. Song,[140] Z. Song,[7] F. Soramel,[29] S. Sorensen,[127] F. Sozzi,[99] E. Spiriti,[73] I. Sputowska,[119] M. Spyropoulou-Stassinaki,[90] J. Stachel,[95] I. Stan,[63] P. Stankus,[86] E. Stenlund,[33] G. Steyn,[66] J. H. Stiller,[95] D. Stocco,[115] P. Strmen,[38] A. A. P. Suaide,[122] T. Sugitate,[47] C. Suire,[52] M. Suleymanov,[16] M. Suljic,[25,*] R. Sultanov,[59] M. Šumbera,[85] S. Sumowidagdo,[50] A. Szabo,[38] I. Szarka,[38] A. Szczepankiewicz,[136] M. Szymanski,[136] U. Tabassam,[16] J. Takahashi,[123] G. J. Tambave,[18] N. Tanaka,[130] M. Tarhini,[52] M. Tariq,[19] M. G. Tarzila,[79] A. Tauro,[35] G. Tejeda Muñoz,[2] A. Telesca,[35] K. Terasaki,[129] C. Terrevoli,[29] B. Teyssier,[132] J. Thäder,[75] D. Thakur,[49] D. Thomas,[120] R. Tieulent,[132] A. Tikhonov,[57] A. R. Timmins,[124] A. Toia,[54] S. Trogolo,[26] G. Trombetta,[32] V. Trubnikov,[3] W. H. Trzaska,[125] T. Tsuji,[129] A. Tumkin,[101] R. Turrisi,[109] T. S. Tveter,[22] K. Ullaland,[18] A. Uras,[132] G. L. Usai,[24] A. Utrobicic,[131] M. Vala,[60] L. Valencia Palomo,[71] J. Van Der Maarel,[58] J. W. Van Hoorne,[35,114] M. van Leeuwen,[58] T. Vanat,[85] P. Vande Vyvre,[35] D. Varga,[138] A. Vargas,[2] M. Vargyas,[125] R. Varma,[48] M. Vasileiou,[90] A. Vasiliev,[81] A. Vauthier,[72] O. Vázquez Doce,[94,36] V. Vechernin,[134] A. M. Veen,[58] A. Velure,[18] E. Vercellin,[26] S. Vergara Limón,[2] R. Vernet,[8] L. Vickovic,[118] J. Viinikainen,[125] Z. Vilakazi,[128] O. Villalobos Baillie,[103] A. Villatoro Tello,[2] A. Vinogradov,[81] L. Vinogradov,[134] T. Virgili,[30] V. Vislavicius,[33] Y. P. Viyogi,[135] A. Vodopyanov,[67] M. A. Völkl,[95] K. Voloshin,[59] S. A. Voloshin,[137] G. Volpe,[32,138] B. von Haller,[35] I. Vorobyev,[94,36] D. Vranic,[99,35] J. Vrláková,[40] B. Vulpescu,[71] B. Wagner,[18] J. Wagner,[99] H. Wang,[58] M. Wang,[7] D. Watanabe,[130] Y. Watanabe,[129] M. Weber,[35,114] S. G. Weber,[99] D. F. Weiser,[95] J. P. Wessels,[55] U. Westerhoff,[55] A. M. Whitehead,[91] J. Wiechula,[34] J. Wikne,[22] G. Wilk,[78] J. Wilkinson,[95] G. A. Willems,[55] M. C. S. Williams,[106] B. Windelband,[95] M. Winn,[95] S. Yalcin,[70] P. Yang,[7] S. Yano,[47] Z. Yin,[7] H. Yokoyama,[130] I.-K. Yoo,[98] J. H. Yoon,[51] V. Yurchenko,[3] A. Zaborowska,[136] V. Zaccolo,[82] A. Zaman,[16] C. Zampolli,[106,35] H. J. C. Zanoli,[122] S. Zaporozhets,[67] N. Zardoshti,[103] A. Zarochentsev,[134] P. Závada,[61] N. Zaviyalov,[101] H. Zbroszczyk,[136] I. S. Zgura,[63] M. Zhalov,[87] H. Zhang,[18,7] X. Zhang,[75,7] Y. Zhang,[7] C. Zhang,[58] Z. Zhang,[7] C. Zhao,[22] N. Zhigareva,[59] D. Zhou,[7] Y. Zhou,[82] Z. Zhou,[18] H. Zhu,[18,7] J. Zhu,[7,115] A. Zichichi,[27,12] A. Zimmermann,[95] M. B. Zimmermann,[55,35] G. Zinovjev,[3] and M. Zyzak[42]

(ALICE Collaboration)

[1]*A. I. Alikhanyan National Science Laboratory (Yerevan Physics Institute) Foundation, Yerevan, Armenia*
[2]*Benemérita Universidad Autónoma de Puebla, Puebla, Mexico*
[3]*Bogolyubov Institute for Theoretical Physics, Kiev, Ukraine*
[4]*Bose Institute, Department of Physics and Centre for Astroparticle Physics and Space Science (CAPSS), Kolkata, India*
[5]*Budker Institute for Nuclear Physics, Novosibirsk, Russia*
[6]*California Polytechnic State University, San Luis Obispo, California 93407, USA*
[7]*Central China Normal University, Wuhan, China*
[8]*Centre de Calcul de l'IN2P3, Villeurbanne, France*
[9]*Centro de Aplicaciones Tecnológicas y Desarrollo Nuclear (CEADEN), Havana, Cuba*
[10]*Centro de Investigaciones Energéticas Medioambientales y Tecnológicas (CIEMAT), Madrid, Spain*
[11]*Centro de Investigación y de Estudios Avanzados (CINVESTAV), Mexico City and Mérida, Mexico*
[12]*Centro Fermi-Museo Storico della Fisica e Centro Studi e Ricerche "Enrico Fermi," Rome, Italy*
[13]*Chicago State University, Chicago, Illinois 60628, USA*
[14]*China Institute of Atomic Energy, Beijing, China*
[15]*Commissariat à l'Energie Atomique, IRFU, Saclay, France*
[16]*COMSATS Institute of Information Technology (CIIT), Islamabad, Pakistan*
[17]*Departamento de Física de Partículas and IGFAE, Universidad de Santiago de Compostela, Santiago de Compostela, Spain*
[18]*Department of Physics and Technology, University of Bergen, Bergen, Norway*
[19]*Department of Physics, Aligarh Muslim University, Aligarh, India*
[20]*Department of Physics, Ohio State University, Columbus, Ohio 43210, USA*

[21]*Department of Physics, Sejong University, Seoul, South Korea*
[22]*Department of Physics, University of Oslo, Oslo, Norway*
[23]*Dipartimento di Fisica dell'Università "La Sapienza" and Sezione INFN Rome, Italy*
[24]*Dipartimento di Fisica dell'Università and Sezione INFN, Cagliari, Italy*
[25]*Dipartimento di Fisica dell'Università and Sezione INFN, Trieste, Italy*
[26]*Dipartimento di Fisica dell'Università and Sezione INFN, Turin, Italy*
[27]*Dipartimento di Fisica e Astronomia dell'Università and Sezione INFN, Bologna, Italy*
[28]*Dipartimento di Fisica e Astronomia dell'Università and Sezione INFN, Catania, Italy*
[29]*Dipartimento di Fisica e Astronomia dell'Università and Sezione INFN, Padova, Italy*
[30]*Dipartimento di Fisica 'E.R. Caianiello' dell'Università and Gruppo Collegato INFN, Salerno, Italy*
[31]*Dipartimento di Scienze e Innovazione Tecnologica dell'Università del Piemonte Orientale and Gruppo Collegato INFN, Alessandria, Italy*
[32]*Dipartimento Interateneo di Fisica "M. Merlin" and Sezione INFN, Bari, Italy*
[33]*Division of Experimental High Energy Physics, University of Lund, Lund, Sweden*
[34]*Eberhard Karls Universität Tübingen, Tübingen, Germany*
[35]*European Organization for Nuclear Research (CERN), Geneva, Switzerland*
[36]*Excellence Cluster Universe, Technische Universität München, Munich, Germany*
[37]*Faculty of Engineering, Bergen University College, Bergen, Norway*
[38]*Faculty of Mathematics, Physics and Informatics, Comenius University, Bratislava, Slovakia*
[39]*Faculty of Nuclear Sciences and Physical Engineering, Czech Technical University in Prague, Prague, Czech Republic*
[40]*Faculty of Science, P.J. Šafárik University, Košice, Slovakia*
[41]*Faculty of Technology, Buskerud and Vestfold University College, Vestfold, Norway*
[42]*Frankfurt Institute for Advanced Studies, Johann Wolfgang Goethe-Universität Frankfurt, Frankfurt, Germany*
[43]*Gangneung-Wonju National University, Gangneung, South Korea*
[44]*Department of Physics, Gauhati University, Guwahati, India*
[45]*Helmholtz-Institut für Strahlen- und Kernphysik, Rheinische Friedrich-Wilhelms-Universität Bonn, Bonn, Germany*
[46]*Helsinki Institute of Physics (HIP), Helsinki, Finland*
[47]*Hiroshima University, Hiroshima, Japan*
[48]*Indian Institute of Technology Bombay (IIT), Mumbai, India*
[49]*Indian Institute of Technology Indore (IITI), Indore, India*
[50]*Indonesian Institute of Sciences, Jakarta, Indonesia*
[51]*Inha University, Incheon, South Korea*
[52]*Institut de Physique Nucléaire d'Orsay (IPNO), Université Paris-Sud, CNRS-IN2P3, Orsay, France*
[53]*Institut für Informatik, Johann Wolfgang Goethe-Universität Frankfurt, Frankfurt, Germany*
[54]*Institut für Kernphysik, Johann Wolfgang Goethe-Universität Frankfurt, Frankfurt, Germany*
[55]*Institut für Kernphysik, Westfälische Wilhelms-Universität Münster, Münster, Germany*
[56]*Institut Pluridisciplinaire Hubert Curien (IPHC), Université de Strasbourg, CNRS-IN2P3, Strasbourg, France*
[57]*Institute for Nuclear Research, Academy of Sciences, Moscow, Russia*
[58]*Institute for Subatomic Physics of Utrecht University, Utrecht, Netherlands*
[59]*Institute for Theoretical and Experimental Physics, Moscow, Russia*
[60]*Institute of Experimental Physics, Slovak Academy of Sciences, Košice, Slovakia*
[61]*Institute of Physics, Academy of Sciences of the Czech Republic, Prague, Czech Republic*
[62]*Institute of Physics, Bhubaneswar, India*
[63]*Institute of Space Science (ISS), Bucharest, Romania*
[64]*Instituto de Ciencias Nucleares, Universidad Nacional Autónoma de México, Mexico City, Mexico*
[65]*Instituto de Física, Universidad Nacional Autónoma de México, Mexico City, Mexico*
[66]*iThemba LABS, National Research Foundation, Somerset West, South Africa*
[67]*Joint Institute for Nuclear Research (JINR), Dubna, Russia*
[68]*Konkuk University, Seoul, South Korea*
[69]*Korea Institute of Science and Technology Information, Daejeon, South Korea*
[70]*KTO Karatay University, Konya, Turkey*
[71]*Laboratoire de Physique Corpusculaire (LPC), Clermont Université, Université Blaise Pascal, CNRS-IN2P3, Clermont-Ferrand, France*
[72]*Laboratoire de Physique Subatomique et de Cosmologie, Université Grenoble-Alpes, CNRS-IN2P3, Grenoble, France*
[73]*Laboratori Nazionali di Frascati, INFN, Frascati, Italy*
[74]*Laboratori Nazionali di Legnaro, INFN, Legnaro, Italy*
[75]*Lawrence Berkeley National Laboratory, Berkeley, California 94720, USA*
[76]*Moscow Engineering Physics Institute, Moscow, Russia*
[77]*Nagasaki Institute of Applied Science, Nagasaki, Japan*
[78]*National Centre for Nuclear Studies, Warsaw, Poland*
[79]*National Institute for Physics and Nuclear Engineering, Bucharest, Romania*

[80]*National Institute of Science Education and Research, Bhubaneswar, India*
[81]*National Research Centre Kurchatov Institute, Moscow, Russia*
[82]*Niels Bohr Institute, University of Copenhagen, Copenhagen, Denmark*
[83]*Nikhef, Nationaal instituut voor subatomaire fysica, Amsterdam, Netherlands*
[84]*Nuclear Physics Group, STFC Daresbury Laboratory, Daresbury, United Kingdom*
[85]*Nuclear Physics Institute, Academy of Sciences of the Czech Republic, Řež u Prahy, Czech Republic*
[86]*Oak Ridge National Laboratory, Oak Ridge, Tennessee 37831, USA*
[87]*Petersburg Nuclear Physics Institute, Gatchina, Russia*
[88]*Physics Department, Creighton University, Omaha, Nebraska 68102, USA*
[89]*Physics Department, Panjab University, Chandigarh, India*
[90]*Physics Department, University of Athens, Athens, Greece*
[91]*Physics Department, University of Cape Town, Cape Town, South Africa*
[92]*Physics Department, University of Jammu, Jammu, India*
[93]*Physics Department, University of Rajasthan, Jaipur, India*
[94]*Physik Department, Technische Universität München, Munich, Germany*
[95]*Physikalisches Institut, Ruprecht-Karls-Universität Heidelberg, Heidelberg, Germany*
[96]*Politecnico di Torino and Sezione INFN, Turin, Italy*
[97]*Purdue University, West Lafayette, Indiana 47907, USA*
[98]*Pusan National University, Pusan, South Korea*
[99]*Research Division and ExtreMe Matter Institute EMMI, GSI Helmholtzzentrum für Schwerionenforschung, Darmstadt, Germany*
[100]*Rudjer Bošković Institute, Zagreb, Croatia*
[101]*Russian Federal Nuclear Center (VNIIEF), Sarov, Russia*
[102]*Saha Institute of Nuclear Physics, Kolkata, India*
[103]*School of Physics and Astronomy, University of Birmingham, Birmingham, United Kingdom*
[104]*Sección Física, Departamento de Ciencias, Pontificia Universidad Católica del Perú, Lima, Peru*
[105]*Sezione INFN, Bari, Italy*
[106]*Sezione INFN, Bologna, Italy*
[107]*Sezione INFN, Cagliari, Italy*
[108]*Sezione INFN, Catania, Italy*
[109]*Sezione INFN, Padova, Italy*
[110]*Sezione INFN, Rome, Italy*
[111]*Sezione INFN, Trieste, Italy*
[112]*Sezione INFN, Turin, Italy*
[113]*SSC IHEP of NRC Kurchatov institute, Protvino, Russia*
[114]*Stefan Meyer Institut für Subatomare Physik (SMI), Vienna, Austria*
[115]*SUBATECH, Ecole des Mines de Nantes, Université de Nantes, CNRS-IN2P3, Nantes, France*
[116]*Suranaree University of Technology, Nakhon Ratchasima, Thailand*
[117]*Technical University of Košice, Košice, Slovakia*
[118]*Technical University of Split FESB, Split, Croatia*
[119]*The Henryk Niewodniczanski Institute of Nuclear Physics, Polish Academy of Sciences, Cracow, Poland*
[120]*Physics Department, The University of Texas at Austin, Austin, Texas 78712, USA*
[121]*Universidad Autónoma de Sinaloa, Culiacán, Mexico*
[122]*Universidade de São Paulo (USP), São Paulo, Brazil*
[123]*Universidade Estadual de Campinas (UNICAMP), Campinas, Brazil*
[124]*University of Houston, Houston, Texas 77004, USA*
[125]*University of Jyväskylä, Jyväskylä, Finland*
[126]*University of Liverpool, Liverpool, United Kingdom*
[127]*University of Tennessee, Knoxville, Tennessee 37996, USA*
[128]*University of the Witwatersrand, Johannesburg, South Africa*
[129]*University of Tokyo, Tokyo, Japan*
[130]*University of Tsukuba, Tsukuba, Japan*
[131]*University of Zagreb, Zagreb, Croatia*
[132]*Université de Lyon, Université Lyon 1, CNRS/IN2P3, IPN-Lyon, Villeurbanne, France*
[133]*Università di Brescia*
[134]*V. Fock Institute for Physics, St. Petersburg State University, St. Petersburg, Russia*
[135]*Variable Energy Cyclotron Centre, Kolkata, India*
[136]*Warsaw University of Technology, Warsaw, Poland*
[137]*Wayne State University, Detroit, Michigan 48202, USA*
[138]*Wigner Research Centre for Physics, Hungarian Academy of Sciences, Budapest, Hungary*

[139]*Yale University, New Haven, Connecticut 06520, USA*
[140]*Yonsei University, Seoul, South Korea*
[141]*Zentrum für Technologietransfer und Telekommunikation (ZTT), Fachhochschule Worms, Worms, Germany*

[*]Deceased.
[†]Also at Georgia State University, Atlanta, Georgia 30302, USA.
[‡]Also at Department of Applied Physics, Aligarh Muslim University, Aligarh, India.
[§]Also at M.V. Lomonosov Moscow State University, D. V. Skobeltsyn Institute of Nuclear, Physics, Moscow, Russia.